Effects of Rain on the Ocean Radar Backscatter at Near-Nadir Incidence Angles: Insights From the Ku-Band SWIM/CFOSAT Under Low to Strong Wind Observations

Xiaolu Zhao, Biao Zhang, *Senior Member, IEEE*, Ludivine Oruba, Alexis Mouche, and Danièle Hauser, *Senior Member, IEEE*

***Abstract*—The surface wave investigation and monitoring (SWIM) instrument, onboard China and France Oceanography Satellite (CFOSAT), is a Ku-band real-aperture radar, with six beams that illuminate the ocean surface at near-nadir incidences ranging from 0° to 10°. In this study, we investigate the effect of rain on the normalized radar cross section (NRCS) measured by SWIM under both tropical cyclone (TC) and non-TC conditions. Rain primarily attenuates the radar backscatter from the ocean surface. Under non-TC conditions, when wind speeds are below 21 m/s, the NRCS reduction is small (<1 dB) during light to moderate rain (<5 mm/h), but becomes very significant (>4–5 dB) under heavy rain (>15 mm/h) conditions. The impact of rain generally decreases as wind speed increases, especially at the smallest incidence angle. At low wind speeds, the NRCS reduction is also sensitive to the incidence angle. Based on a simplified model and the differing sensitivities of NRCS to surface roughness at two near-nadir incidence angles, we find that rain also influences the surface signal at incidence angles below 10°, in addition to the dominant effect of atmospheric attenuation, which leads to a consistent NRCS reduction across all wind speeds and incidence angles. Specifically, it contributes positively to NRCS at wind speeds above 7 m/s and negatively at lower wind speeds. This behavior is attributed to increased surface roughness from splashes and ring waves at low wind speeds, and to decreased roughness due to wave damping at moderate and high wind speeds. In TC environments, the NRCS tends to saturate under light to moderate rain rates (<5 mm/h) when wind speeds exceed approximately 35 m/s. In contrast, under heavy rain (>15 mm/h) conditions, the NRCS continues to decrease as wind speed increases. In both TC and non-TC conditions, beyond atmospheric attenuation, the impact of rain on surface roughness must be considered to fully explain the observed NRCS variations with wind and rain rate.**

***Index Terms*—CFOSAT surface wave investigation and monitoring (SWIM), radar backscatter, rain, tropical cyclone (TC).**

I. INTRODUCTION

THE China and France Oceanography Satellite (CFOSAT), a joint mission developed by Chinese and French Space Agencies, was successfully launched on October 29, 2018. The mission is designed to simultaneously characterize ocean surface winds and waves, with the goal of improving sea states predictions and advancing our understanding of air–sea interactions. CFOSAT is equipped with two primary payloads: the surface wave investigation and monitoring (SWIM) and a wind scatterometer, both of which support scientific research and operational applications related to ocean dynamics. SWIM is the first spaceborne wave spectrometer specially dedicated to measuring ocean surface waves by detecting the modulation in the backscattered signal caused by the tilt of surface long waves [1], [2]. SWIM operates at the Ku-band with a frequency of 13.575 GHz, where oceanic rainfall can significantly affect radar returns and potentially introduce systematic errors in both surface wave and wind measurements. However, Zhao et al. [3] demonstrated that during tropical cyclone (TC) Sam (2021), although rain-induced signatures were evident in the normalized radar cross section (NRCS) profiles, the accurate retrieval of wave spectra from SWIM measurements remained feasible across a wide range of wind and rain conditions, provided that the signal remained sufficiently above the noise level. This robustness was attributed to the fact that rain-induced perturbations occur at a spatial scale distinct from the NRCS fluctuations associated with ocean surface waves. However, since NRCS measurements at small incidence angles can also provide valuable information on surface wind fields [4], [5], a quantitative analysis of rain effects on NRCS at these angles is essential for correcting rain-induced contamination

Received 13 March 2025; revised 13 July 2025; accepted 22 July 2025. Date of publication 25 July 2025; date of current version 5 August 2025. This work was supported in part by the National Key Research and Development Program of China under Grant 2024YFC2815703, in part by Hainan Province Science and Technology Special Fund under Grant SOLZSKY2025009, in part by China Scholarship Council (CSC) Ph.D. Joint Training Program under Grant 202109040021, and in part by the Centre National d'Etudes Spatiales (CNES)/Terre, Océan, Surfaces Continentales, Atmosphére (TOSCA) (Maeva Project). *(Corresponding author: Biao Zhang.)*

Xiaolu Zhao is with the State Key Laboratory of Climate System Prediction and Risk Management and the School of Marine Sciences, Nanjing University of Information Science and Technology, Nanjing 210044, China (e-mail: zhaoxiaolu@nuist.edu.cn).

Biao Zhang is with the State Key Laboratory of Climate System Prediction and Risk Management and the School of Marine Sciences, Nanjing University of Information Science and Technology, Nanjing 210044, China, and also with Sanya Oceanographic Laboratory, Sanya 572024, China (e-mail: zhangbiao@nuist.edu.cn).

Ludivine Oruba is with the Laboratoire Atmosphères, Observations Spatiales (LATMOS), CNRS, UVSQ, Sorbonne Université, 78280 Paris, France (e-mail: ludivine.oruba@latmos.ipsl.fr).

Alexis Mouche is with the Institut Francais de Recherche pour l'Exploitation de la Mer (IFREMER), 29280 Plouzané, France (e-mail: Alexis.Mouche@ifremer.fr).

Danièle Hauser is with the Laboratoire Atmosphères, Observations Spatiales (LATMOS/IPSL), CNRS, UVSQ Université Paris-Saclay, Sorbonne Université, 78280 Guyancourt, France (e-mail: daniele.hauser@latmos.ipsl.fr).

Digital Object Identifier 10.1109/TGRS.2025.3592525

and improving the accuracy of remote sensing of ocean surface winds.

Rainfall impacts the ocean surface NRCS through multiple mechanisms. When raindrops impinge onto the ocean surface, they typically create splash products such as craters, crowns, stalks, and secondary droplets ejected from the water, followed by the formation of spreading of ring waves [6], [7]. During a rain event, the resulting turbulence in the upper water layer, dampens short wind-generated gravity waves [8]. In addition to these surface effects, volume scattering and attenuation of electromagnetic waves by atmospheric raindrops (hydrometeors) also affect the radar signal as it propagates through the atmosphere [9]. Overall, rain-induced splash products, ring waves, and downdrafts roughen the ocean surface by modifying the centimeter-scale wave fields [10], [11], [12]. In contrast, subsurface turbulence generated by raindrop can dampen short waves and reduce surface roughness [13], [14]. The net effect on NRCS depends strongly on the radar incidence angle. At moderate incidence angles (25°–70°), variations in surface roughness cause corresponding increases or decreases in NRCS, consistent with Bragg scattering theory. However, at small incidence angles (<10°), where quasi-specular reflection dominates, the relationship is reversed. The scattering behavior of rain-affected ocean surface has been extensively studied [7], [12], [13]. Raindrop-induced splashes typically contribute through non-Bragg scattering, with their effects strongly dependent on both polarization and incidence angle.

The rain interference poses a significant challenge to the accurate retrieval of ocean surface winds from scatterometer data [15] and complicates reliable estimations of significant wave height from altimeter measurements [16], [17], [18]. Consequently, specialized methods are necessary to mitigate the impacts of rain on radar observations. A common approach involves rain flagging, which uses collocated passive microwave data to identify and exclude rain-contaminated measurements or applies quality control procedures that compare observed NRCS with empirically modeled values [19]. In addition, some studies aim to separately simulate the effects of wind and rain, incorporating rain column parameters into retrieval models to compensate for radar signal attenuation caused by rainfall [20].

Previous studies have shown that the effects of rain on the NRCS are strongly dependent on the radar frequency and incidence angle [12], [21]. Scatterometer observations confirm that NRCS at Ku-band is more affected by rain than at C-band [22], primarily due to increased attenuation and volume scattering caused by atmospheric rain. Furthermore, it has been shown that the impact of high rain rates on C-band scatterometer measurements increases with incidence angles between 40° and 57° [23]. At moderate incidence angles, the impact of rain on NRCS has been extensively analyzed using multifrequency and multipolarization scatterometer and synthetic aperture radar (SAR) observations [12], [21], [23], [24], [25], [26], [27], [28], [29], [30]. The significant contribution of rain-induced ring waves has been demonstrated through the measurement of radar returns in a field experiment using scatterometers operating at various frequencies, polarizations, and incidence angles [12]. Analysis of Doppler spectra concluded that Bragg scattering from ring waves is the dominant mechanism responsible for VV-polarized backscatter from the rain-roughened ocean surface [12]. Alpers et al. [24] investigated the physical mechanisms responsible for C-band NRCS signatures associated with rain in SAR images acquired over the ocean. A polarimetric decomposition analysis of a RADARSAT-2 quad-polarization SAR image revealed that the NRCS signature of rain cells is primarily due to surface scattering. The observations also showed significant enhancements in both co- and cross-polarized NRCS, indicating the presence of non-Bragg scattering contributions. Furthermore, they concluded that at C-band, NRCS can either increase or decrease relative to the background levels depending on several factors, including rain rate, wind speed, incidence angle, raindrop distribution, and rain history. To better understand these effects, numerical models based on rain-induced backscatter mechanisms have been developed [20], [31], [32], [33]. These models aim to describe the dependence of NRCS on various factors, including frequency, polarization, incidence angle, rain rate, wind speed, and wind direction.

All of the aforementioned studies have primarily focused on moderate incidences (typically greater than 25°–30°), whereas research on the effects of rain on NRCS at small incidence angles remains relatively limited. Most documented efforts in this regime have concentrated on nadir-viewing satellite altimeter measurements [16], [17], [18], [34]. At both C- and Ku-band frequencies, the dominant impact of rain is the attenuation of the radar signal, with attenuation at Ku-band being approximately an order of magnitude greater than that at C-band. This wavelength-dependent sensitivity enables the potential for retrieving rain rates, along with the NRCS corrected for rain attenuation. Several studies have demonstrated the feasibility of retrieving reliable surface wind, wave, and rain rate parameters under TC conditions using dual-frequency altimeter measurements [17], [18]. For near-nadir observations, the impact of rain on radar backscatter has been assessed by analyzing collocated triplets of NRCS, rain rates from the Tropical Rainfall Mapping Mission (TRMM) Precipitation Radar (PR), and wind speeds from the European Centre for Medium-Range Weather Forecasts (ECMWF) [4]. The results showed that radar backscatter generally decreases with increasing rain rates, and that the magnitude of this effect is strongly modulated by wind speed. However, these analyses were limited to incidence angles between 1° and 6° and wind speeds ranging from 2 to 16 m/s. In addition, various rain-related effects were aggregated into a single parameter, without distinguishing the contributions of individual influencing factors.

In this study, we evaluate the impact of rain on NRCS at near-nadir incidence angles (2°–10°) using SWIM Ku-band radar backscatter measurements collocated with rain rates from both the Global Precipitation Measurement (GPM) products and ground-based Next Generation Weather Radar (NEXRAD) observations. Unlike previous studies based on scatterometer and SAR data that primarily focus on moderate incidence angle, our research targets near-nadir observations, where the relative contributions of atmospheric and surface rain effects differ significantly. By leveraging the differing sensitivities of multiple incidence angles to surface roughness, we propose a simplified modeling approach to separate atmospheric attenuation from rain-induced surface contributions. In contrast to the analysis by Ren et al. [4], our investigation covers a broader incidence angle range (2°–10°) and extends to higher wind speeds (up to 57 m/s), enabled by the incorporation of accurate wind measurements from L-band radiometers under TC conditions. This expanded framework reveals the significant impact of intense rainfall on radar backscatter in TC environments.

Section II describes the CFOSAT SWIM-measured NRCS, along with ancillary data including ECMWF wind fields, rain rates from GPM and NEXRAD, and surface winds derived from L-band radiometers. Section III presents an overview of the results under both non-TC and TC conditions. A detailed discussion is provided in Section IV, and the main findings are summarized in Section V.

II. DATASETS

A. SWIM NRCS and ECMWF Wind Data

The SWIM onboard CFOSAT is a Ku-band real-aperture radar deployed in a polar orbit at an altitude of approximately 519 km, providing global coverage with a 13-day cycle [1]. It sequentially illuminates the ocean surface using six beams, each oriented at a mean incidence angle ranging from 0° to 10° in 2° increment. Each measurement covers a footprint of approximately 18×18 km, with a range resolution in the elevation direction varying between 0.94 and 1.88 m depending on the incidence angle. The radar signal is integrated over the footprint in the direction perpendicular to the elevation plane. Due to its scanning geometry, the observation swath varies with incidence angle, from a radius of approximately 18 km at a 2° to about 90 km at a 10°. Operating at a rotational speed of 5.6 r/min, SWIM samples the full 360° azimuth approximately every 7.5°, ensuring comprehensive directional coverage. The NRCS, after calibration and geolocation with corrections for instrument gain and geometry, is provided in a Level-1A (L1A) product at its original range resolution. The Level 2S (L2S) product further resamples the NRCS at a horizontal resolution of 20 m for each azimuth. In this study, we use resampled NRCS values from the L2S product. Since rainfall is typically inhomogeneous within the footprint, distortions in the NRCS profile along the elevation direction may occur (e.g., see [3, Fig. 10]). To ensure consistency and robustness, we use the mean NRCS values in the footprint. We have verified that our main conclusions remain consistent when using NRCS values taken from the center of the swath. To isolate rain effects accurately, the L2S radar backscatter measurements used in this study are not corrected for the atmospheric attenuation, even though such corrections are available in the AUX-METEO ancillary products.

In addition, ancillary meteorological variables are available from the SWIM along-track AUX-METEO products. Wind fields from the ECMWF are spatially and temporally interpolated to the center of the swath for each azimuth and beam. A comparison of ECMWF winds under various rainy conditions with buoy measurements, as discussed in [15], shows that although the ECMWF reanalysis data tend to underestimate winds speed during rainfall and does not fully capture small-scale wind variability, the biases between ECMWF and buoy winds are considerably less sensitive to rain than the standard deviation. Importantly, the relationship remains approximately linear even for rain rates exceeding 3 mm/h. As we primarily use temporally and spatially averaged ECMWF winds in this study, they are deemed suitable for examining the effects of rain on SWIM measurements under non-TC conditions. As a cross-validation, we also collocated wind data from the Advanced Scatterometer (ASCAT) with SWIM NRCS. The results from ASCAT–SWIM matchups (see the Appendix) are consistent with those obtained from ECMWF–SWIM collocations over the same time periods. However, since the ASCAT-based matchup dataset (ASCAT wind, SWIM NRCS, and rain rate) is more limited in coverage, ECMWF winds are retained for the main analysis.

B. GPM and NEXRAD Rain Rates

The two high-resolution rain rate products used in this study are the Integrated MultisatellitE Retrievals for GPM (IMERG) Version 07 data and dual-polarization NEXRAD observations. The Level-3 IMERG product is derived from intermittent precipitation estimates provided by partner satellites within the GPM constellation. The GPM mission was designed to improve measurements of instantaneous precipitation relative to its predecessor, TRMM, particularly for light rain and cold-season solid precipitation [35]. IMERG precipitation estimates are primarily generated by combining passive microwave and infrared observations, calibrated against microwave-based retrievals. These estimates are further refined through the incorporation of monthly rain gauge data to produce the Final Run product. Distributed by the National Aeronautics and Space Administration (NASA), the IMERG product provides global precipitation estimates at a 30-min temporal resolution and a spatial resolution of $0.1° \times 0.1°$ [36]. In addition to the gauge-calibrated multisatellite precipitation estimates, the product includes a quality index (QI), which serves as an indicator of data reliability. According to the product manual, evaluations using multiradar and multisensor datasets indicate that QI values above 0.6 outperform those below 0.4 in terms of correlation and scatter metrics. Therefore, QI values between 0.6 and 1 are generally recommended for identifying valid precipitation estimates from the current half-hour microwave swath data and short-interval morphing algorithms.

The NEXRAD network consists of 160 high-resolution Doppler weather radars, jointly operated by the National Weather Service, the Federal Aviation Administration, and the U.S. Air Force. Most radars are located in the U.S. territories and the continental United States, with a few stations deployed overseas. Each station utilizes the S-band Weather Surveillance Radar—1988 Doppler (WSR-88D) system to detect atmospheric precipitation and wind fields. The National Centers for Environmental Information (NCEI) of the National Atmospheric Administration (NOAA) routinely distributes more than 75 Level-III products, including base and composite reflectivity, storm-relative velocity, and 1- and 3-h precipitation estimates. Due to their high temporal resolution and wide spatial coverage, we used archived Level-III base reflectivity data from 34 coastal NEXRAD stations instead of the standard hourly precipitation estimates. These data are recorded according at radar scan intervals of approximately 4.5, 5, 6, or 10 min, depending on the selected volume coverage pattern. The reflectivity data have a spatial resolution of 1° in azimuth and 1 km in range, with a maximum detection radius of 460 km. Rain rates R are estimated from the reflectivity using the empirical relationship. By default, the relationship $Z_{\text{lin}} = 300R^{1.4}$ is applied, where Z_{lin} is the reflectivity in linear scale (not in dBZ) [37]. For tropical convective systems, a modified relation $Z_{\text{lin}} = 250R^{1.2}$ is used to better account for the differing microphysical properties of rainfall in such environments [38].

C. Microwave Radiometer Surface Wind Speeds

The Soil Moisture and Ocean Salinity (SMOS) satellite, operated by the European Space Agency (ESA), was launched in November 2009. Following its success, NASA launched the Soil Moisture Active Passive (SMAP) satellite, which began operations in April 2015, three months after its launch. Both missions employ L-band radiometers operating at 1.4 GHz to measure microwave emissions, providing valuable observations of surface wind speeds, particularly under extreme conditions. A key advantage of the L-band radiometer is its reduced sensitivity to atmospheric effects, rainfall, and sea spray, making it especially suitable for observing ocean surface winds in high wind and rainy environments [39]. SMOS and SMAP are both deployed in near-polar orbits, with SMOS orbiting at a mean altitude of approximately 755 km and SMAP at 685 km. Each satellite provides brightness temperature images over a swath of approximately 1000 km, with a nominal spatial resolution of about 40 km. The wide swath coverage enables near-global observations every three days for SMOS and every eight days for SMAP.

In this study, we use the SMOS Near-Real Time (NRT) Level 2 swath wind speed products, available upon registration at https://smos-diss.eo.esa.int/oads/access/. These products provide gridded surface wind speeds at a spatial resolution of 0.25° × 0.25°, including data from both ascending and descending orbital passes. However, wind speed estimates below 5 m/s may be unreliable due to a discontinuity in the wind probability density function (pdf) near 1.5 m/s. For wind speeds exceeding TC force (>32 m/s), comparisons with SMAP data indicate that SMOS NRT wind speeds tend to be slightly underestimated, with a root mean square error (RMSE) of approximately 3.6 m/s. Only SMOS NRT wind data with a quality level (QL) of 0 or 1 are recommended for use; data with QL = 2 should be interpreted with caution. As a supplementary source, we also incorporate SMAP Version 1.0 wind data from remote sensing systems. These Level 3 products provide uniformly gridded (0.25°) daily surface wind speeds, consisting of both ascending and descending passes [40]. For wind speeds above 25 m/s, SMAP wind estimates show good agreement with collocated measurements from the Stepped Frequency Microwave Radiometer (SFMR), with a standard deviation of approximately 3 m/s [41]. Both the SMOS and SMAP datasets are particularly suitable for wind speeds exceeding 12 m/s, as L-band emissivity signals from foam layers become detectable only when foam layer thickness exceeds approximately 10 cm, which typically occurs at wind speeds above this threshold [39].

D. TC Best-Track Data

The TC tracks used in this study are obtained from the International Best Track Archive for Climate Stewardship (IBTrACS) dataset [42], [43], which is compiled through collaboration with all World Meteorological Organization Regional Specialized Meteorological Centres, as well as contributions from other agencies and individuals worldwide. We use version v04r01 of the IBTrACS database, which provides 3-hourly summaries of key storm parameters, including storm center positions, maximum sustained wind speed, and minimum sea level pressure. To address potential inconsistencies in storm characteristics reported by different contributing agencies, we prioritize data provided by the U.S. Agency.

E. SWIM TC and Non-TC Datasets

To facilitate the analysis of NRCS signatures in the presence of rain under both moderate and severe sea states, two datasets were constructed based on the observations described above. The first dataset consists of SWIM NRCS measurements acquired under rainy but non-TC conditions, spanning the period from January 2021 to December 2022. The second dataset includes NRCS measurements along CFOSAT tracks intersecting TCs, covering January 2021 to December 2023, to ensure sufficient sampling under TC conditions. Prior to data collocation, several quality control criteria were implemented to retain only the most reliable SWIM observations. Specifically, averaged linear NRCS values below the Noise-Equivalent Sigma Zero (NESZ) were excluded. The NESZ profile was derived from SWIM L1A data collected between October 1 and October 7, 2021, yielding average linear NESZ values of 0.52, 0.41, 0.28, 0.21, and 0.46 for incidence angles of 10°, 8°, 6°, 4°, and 2°, respectively. Furthermore, only SWIM measurements located more than 50 km from the coastline and within ±1° of the nominal incidence angle were retained.

The non-TC dataset was constructed through the following procedure. To avoid contamination from sea-ice, SWIM observations were restricted to latitudes between 55°N and 55°S. CFOSAT nadir tracks intersecting with the spatial coverage of GPM gridded products and NEXRAD observations were identified using a 30-min temporal matching window. Rain rates from both NEXRAD and GPM, along with their QI values, were interpolated using cubic interpolation to align with the SWIM NRCS measurements at the center of each swath for the near-nadir beams. Only GPM rain rates with QI values greater than 0.6 were retained for analysis. For the ground-based NEXRAD data, overlapping coverage frequently occurred due to the high density of stations. In cases where multiple precipitation estimates were available for a single

SWIM measurement, the rain rate at the nearest time was selected. The final non-TC dataset consists of approximately 544.8 million collocated data pairs, of which 451.8 million (82.9%) correspond to clear-sky conditions and 93.0 million (17.1%) to various rainfall scenarios.

For SWIM acquisitions during TC conditions, the dataset was constructed as follows. CFOSAT nadir tracks were limited to regions within a 500 km radius of the TC trajectory, and only satellite passes occurring within ±1.5 h of the reported storm's position time were included. Rain rate and wind speed observations were matched using temporal windows of 0.5 and 1.5 h, respectively, and were cubically interpolated to the center of the SWIM swath. The same interpolation scheme described previously was applied to GPM and NEXRAD rain rates. For SMOS wind speed data, only measurements with QL values of 0 or 1 were retained. When both SMOS and SMAP wind data were available for the same location, the dataset with the shorter time difference from the SWIM acquisition was selected, due to the typically large temporal gaps between SMOS and SMAP overpasses. A total of 213 TCs observed by SWIM between 2021 and 2023 were matched with corresponding precipitation and wind field data, resulting in 635330 collocation pairs. Of these, 363 978 (57.3%) were classified as rain-free and 271 352 (42.7%) as rain-affected. In both datasets, the majority of rain rate measurements were derived from GPM observations.

III. RESULTS

A. *NRCS Signatures of Rain Under Non-TC Conditions*

This section first illustrates the impact of rain on NRCS at a 10° incidence angle using selected case studies under varying wind speeds and rain rates. Subsequently, the analysis is then extended to the full collocated dataset from 2011 to 2022 to evaluate the impact of rain on SWIM measurements across near-nadir incidence angles ranging from 2° to 10°.

1) Case Study: In the following examples, SWIM NRCS signatures under rainy conditions are analyzed using collocated NEXRAD observations. The selected cases represent a range of rainfall intensities, from light (see Fig. 1) to moderate (see Fig. 2) and heavy precipitation (see Fig. 3).

Fig. 1 presents two cases of low-intensity rain events observed under low (4–7 m/s) and moderate (12–15 m/s) wind speed conditions. In Fig. 1(a), SWIM radar backscatter at a 10° incidence angle for a subscene was collected during one full antenna rotation (i.e., a 360° clockwise sweep of the off-nadir beam starting from approximately 0° radar azimuth, aligned with true North). This measurement was acquired during a descending CFOSAT pass on July 28, 2021, from 17:55:00 to 17:55:10 UTC. A collocated NEXRAD reflectivity image acquired at 17:55:40 UTC on the same day provides the corresponding rain rate field [shown in color in Fig. 1(a)]. Fig. 1(b) shows the variations of mean SWIM NRCS from the 10° beam as a function of azimuth angle, where positive azimuth is measured clockwise from true North. The magenta and blue curves indicate ECMWF wind speed and NEXRAD rain rate, respectively. At a radar azimuth of 296°, where the rain rate reaches approximately 1.5 mm/h, the NRCS shows a decrease of about 1.0 dB within the rain cell. Although the wind speed in the same region (azimuth >280°) decreases from 6.3 to 3.4 m/s, this variation does not seem to have a significant effect on the NRCS. Nearly identical NRCS values

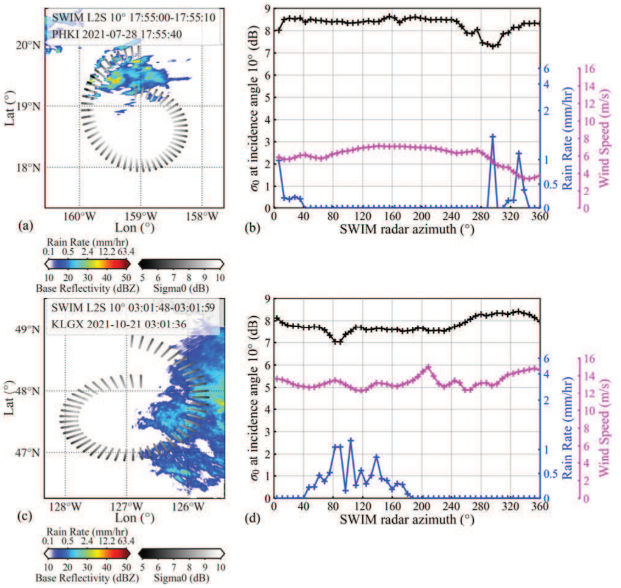

Fig. 1. CFOSAT SWIM observations at a 10° incidence angle during rain events with low rain rates, acquired over one complete antenna rotation. (a) SWIM NRCS acquired near the Hawaiian Islands on July 28, 2021, from 17:55:00 to 17:55:10 UTC, overlaid with collocated NEXRAD reflectivity at 17:55:40 UTC. (c) SWIM NRCS acquired near U.S. West Coast on October 21, 2021, from 03:01:48 to 03:01:59 UTC, with corresponding NEXRAD reflectivity at 03:01:36 UTC. (b) and (d) Azimuthal profiles of mean SWIM NRCS (black), NEXRAD rain rate (blue), and ECMWF wind speed (magenta) corresponding to (a) and (c), respectively.

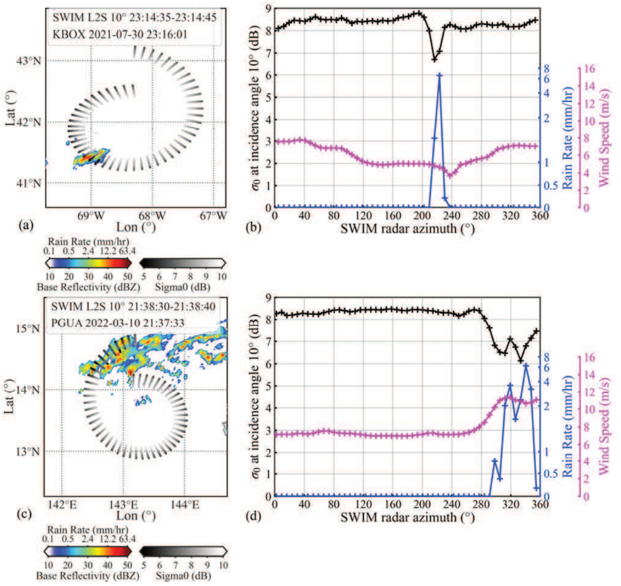

Fig. 2. CFOSAT SWIM observations at a 10° incidence angle during rain events with moderate rain rates, acquired over one complete antenna rotation. (a) SWIM NRCS acquired off U.S. East Coast on July 30, 2021, from 23:14:35 to 23:14:45 UTC, overlaid with collocated NEXRAD reflectivity at 23:16:01 UTC. (c) SWIM NRCS acquired near Northwest Pacific coasts on March 10, 2022, from 21:38:30 to 21:38:40 UTC, with corresponding NEXRAD reflectivity at 21:37:33 UTC. (b) and (d) Azimuthal profiles of mean SWIM NRCS (black), NEXRAD rain rate (blue), and ECMWF wind speed (magenta) corresponding to (a) and (c), respectively.

are observed outside the rain-affected area, despite these wind speed differences. This weak sensitivity of NRCS at a 10° incidence angle to moderate wind speed variation is consistent with previous findings (see [2] and Section III-A2).

Fig. 1(c) presents a second case under low rain rate conditions. SWIM observations were acquired during an ascending CFOSAT pass on October 21, 2021, from 03:01:48 to 03:01:59 UTC, with the corresponding NEXRAD reflectivity image obtained shortly before, at 03:01:36 UTC. The radar image reveals a light rain area extending southward from the coastline, with most collocated rain rates remaining below 1 mm/h. As shown in Fig. 1(d), this rain-affected region spans azimuth angles from 47° to 181°. Within this azimuth intervals, the ECMWF wind speed remains relatively steady at approximately 13 m/s. In this case, the SWIM NRCS shows a decrease of about 1 dB at the location of peak rainfall. However, when the rain rate is less than or equal to 0.5 mm/h, the NRCS remains nearly unchanged, indicating that a very light rain has a negligible impact on radar backscatter under moderate wind conditions.

Fig. 2 presents two cases characterized by moderate rain rates. In Fig. 2(a), SWIM observations were acquired off the U.S. East Coast on July 30, 2021, from 23:14:35 to 23:14:45 UTC, with the corresponding NEXRAD reflectivity image acquired at 23:16:01 UTC. A distinct rain cell is observed, with a maximum rain rate of 6.5 mm/h at a radar azimuth angle of 223°. The ambient wind speed during this event was relatively weak, approximately 4.6 m/s. As shown in Fig. 2(b), the NRCS profile exhibits a pronounced decrease of about 2 dB within the rain cell compared to adjacent clear-sky regions. Fig. 2(c) presents SWIM observations at a 10° incidence angle near the northwest Pacific coast, acquired on March 10, 2022, from 21:38:30 to 21:38:40 UTC. The collocated NEXRAD reflectivity image, obtained at 21:37:33 UTC, shows spatially variable reflectivity indicative of rain. Within the azimuth angle range of 298°–347°, rain rates vary between 0.4 and 6.2 mm/h, and wind speeds increase from 8 m/s to approximately 11 m/s, as shown in Fig. 2(d). A scan along this azimuth sector reveals an NRCS reduction of roughly 2 dB in the rain-affected region.

Fig. 3 presents two rain events characterized by high rain rates. In Fig. 3(a), SWIM observations were acquired over the Atlantic Ocean off the U.S. East Coast on May 7, 2021, from 12:30:56 to 12:31:07 UTC, with the corresponding NEXRAD reflectivity image obtained at 12:31:47 UTC. The top panels display a broad rain zone, with rain rates ranging from 0 to 27 mm/h across radar azimuth angles between 248° and 325°. During this event, ambient wind speeds are weak, ranging from 1 to 5 m/s. Under clear-sky conditions, the mean NRCS at the 10° incidence angle remain stable around 8.5 dB, indicating limited sensitivity to wind speed variations. As the SWIM antenna scans into the rainy area, the NRCS gradually decrease, reaching a minimum of 6.4 dB at the location of peak rainfall intensity. Fig. 3(c) shows another case based on SWIM observations acquired off the U.S. East Coast on July 10, 2022, from 12:22:44 to 12:22:55 UTC. The corresponding NEXRAD reflectivity image, acquired quasi-simultaneously at 12:22:51 UTC, reveals an extensive rain band oriented in a northeast-southwest direction, intersecting the full 360° SWIM scan. According to ECMWF data, ambient wind speeds during this event range from 10 to 11 m/s. As shown in Fig. 3(d), the NRCS profile exhibits four distinct drops corresponding to the rain band. The most pronounced decrease, approximately 3 dB, occurs at a radar azimuth angle of 18°, aligning with the area of maximum rain rate (36.6 mm/h).

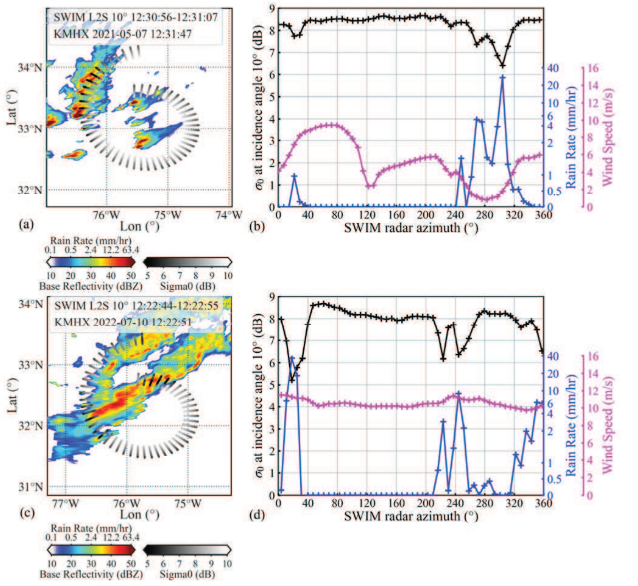

Fig. 3. CFOSAT SWIM observations at a 10° incidence angle during rain events with high rain rates, acquired over one complete antenna rotation. (a) SWIM NRCS acquired off U.S. East Coast on May 7, 2021, from 12:30:56 to 12:31:07 UTC, overlaid with collocated NEXRAD reflectivity at 12:31:47 UTC. (c) SWIM NRCS acquired off U.S. East Coast on July 10, 2022, from 12:22:44 to 12:22:55 UTC, with corresponding NEXRAD reflectivity at 12:22:51 UTC. (b) and (d) Azimuthal profiles of mean SWIM NRCS (black), NEXRAD rain rate (blue), and ECMWF wind speed (magenta) corresponding to (a) and (c), respectively.

Across the six case studies, it is evident that rainfall consistently reduces the SWIM NRCS at a 10° incidence angle under low to moderate wind conditions, regardless of variations in collocated wind speeds. In high rain rate scenarios, the maximum observed NRCS reduction reaches approximately 3 dB at a rain rate of about 37 mm/h. In contrast, when rain rates are below 0.5 mm/h, the impact of rain on NRCS is minimal and often indistinguishable in the NRCS profiles.

2) Statistics Study: In addition to the case studies, we conduct a statistical analysis of ocean surface radar backscatter under varying wind speeds, wind directions, incidence angles, and rain rates to further evaluate the impact of rain on NRCS measurements from CFOSAT SWIM. Fig. 4 illustrates the distribution of NRCS as a function of ECMWF wind speed under rain-free conditions for incidence angles of 2°, 4°, 6°, 8°, and 10°, with a relative wind direction of 180° (i.e., downwind viewing). The black dashed lines denote NRCS values derived from the mode of the pdf, while the black solid lines represent the weighted averages. The wind speed bin width is 1.2 m/s. For an incidence angle of 8° or less, NRCS decreases as wind speed increases. This behavior aligns with the expected reduction in specular reflection due to enhanced surface roughness under higher winds. At a 10° incidence angle, however, the NRCS remains nearly constant over the

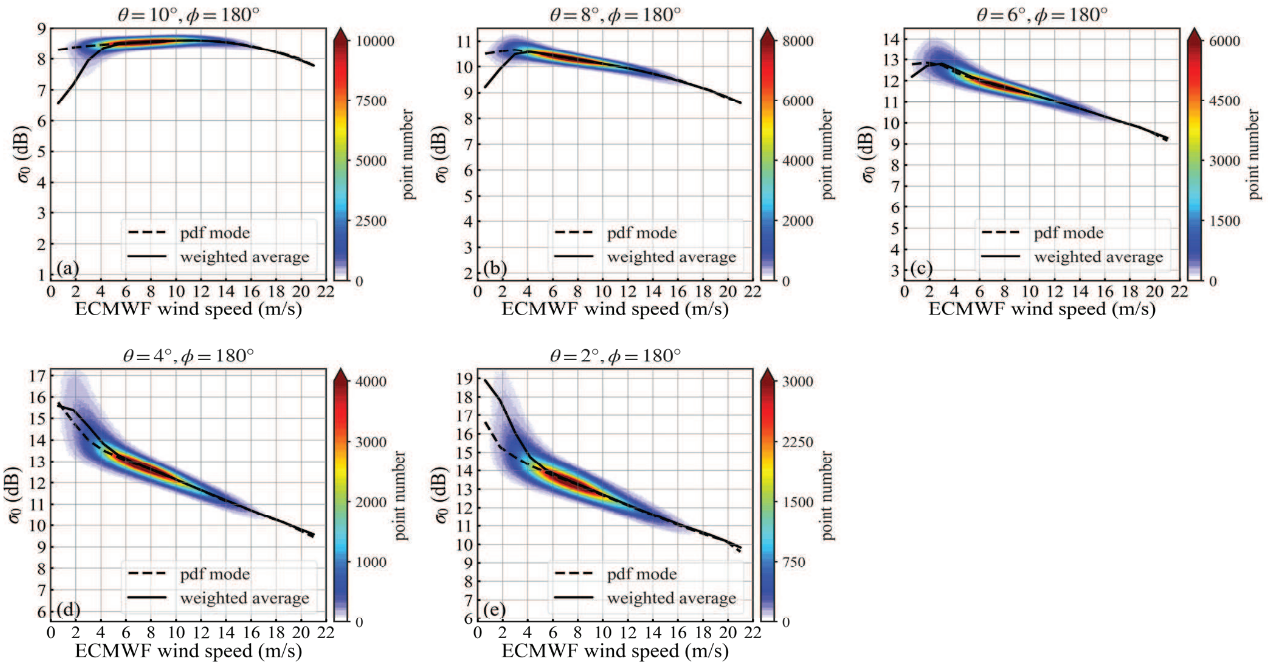

Fig. 4. Distribution of SWIM NRCS under rain-free conditions as a function of ECMWF wind speed, at incidence angles of (a) 10°, (b) 8°, (c) 6°, (d) 4°, and (e) 2°. The black dashed lines represent NRCS values derived from the mode of pdf, while the black solid lines represent the weighted averages.

wind speed range of 4–14 m/s. Notable discrepancies between the pdf mode and the weighted averages are observed at wind speeds below 4 m/s, primarily due to the presence of NRCS outliers that are challenging to filter effectively. In subsequent analyses, the weighted average is adopted as the preferred metric, as it is less sensitive to outliers, particularly at moderate wind speeds and under moderate to high rain rates. The trends observed in Fig. 4 are generally consistent with those reported in [2], although some differences arise due to variations in data processing. Specifically, this study does not apply an atmospheric attenuation correction and uses spatial averaging over the footprint, whereas [2] performs averaging within 0.5° incidence bins.

Fig. 5 presents the comparisons of mean NRCS values at incidence angles ranging from 2° to 10° (in 2° increments) against ECMWF wind speeds under both rain-free conditions (RR =0 mm/h) and across three rain rate categories: $0.5 \leq$ RR <5 mm/h, $5 \leq$ RR <15 mm/h, and RR ≥ 15 mm/h. All cases correspond to a relative wind direction of 180° (downwind viewing). Weighted averages were calculated within 2 m/s wind speed bins, with the error bars indicating the standard deviation of NRCS within each bin. Across all incidence angles, rain generally leads to a reduction in SWIM NRCS values, with greater decreases observed at higher rain rates. For the lowest rain rate category ($0.5 \leq$ RR <5 mm/h), NRCS decreases by less than 0.7 dB when wind speeds exceed 5 m/s. At the highest rain rates (RR $\geq$ 15 mm/h), the reductions become more pronounced. For example, at a 10° incidence angle, NRCS decreases by approximately 2.6 dB for wind speeds between 3 and 13 m/s, and about 2.1 dB at higher wind speeds, as shown in Fig. 5(a). Fig. 5(b) and (c) shows similar trends at 8° and 6° incidence angles, where NRCS reductions reach up to 2.8 and 3.4 dB at a wind speed of 3 m/s, respectively. As wind speed increases to 17 m/s, the reductions reach approximately 2.1 and 1.5 dB, respectively. At lower incidence angles, the impact of rain is even more pronounced. For example, at a 4° incidence angle, the NRCS reduction caused by heavy rain decreases from 4.6 dB at 1 m/s to 1.5 dB at 17 m/s, as shown in Fig. 5(d). Fig. 5(e) shows the reduction ranges from 6.4 to 1.3 dB at a 2° incidence angle over the same wind speed interval. Overall, the magnitude of NRCS reduction due to rain decreases with increasing wind speed. This behavior is further explored by examining the ratio of NRCS values under rain-free and rainy conditions (see below). An exception to this general trend occurs at 8° and 10° incidence angles under very light wind (~1 m/s) and light to moderate rain ($0.5 \leq$ RR <5 mm/h) conditions, where a slight increase in NRCS is observed, as shown in Fig. 5(a) and (b).

While Fig. 5 presents NRCS observations in the downwind direction, Fig. 6 illustrates the relatively small influence of the antenna look direction on the mean NRCS. Specifically, it shows the mean NRCS as a function of the relative wind direction (i.e., the angle between the SWIM antenna look direction and the wind direction) for a fixed wind speed of 10 m/s. At a 10° incidence angle, a noticeable azimuthal asymmetry is observed under rain-free conditions. The NRCS peaks in the downwind direction and reaches a minimum in the crosswind direction, with a crosswind-to-downwind NRCS difference of approximately 0.5 dB. The upwind-to-downwind difference is slightly smaller, around 0.4 dB. This asymmetry initially decreases as wind speed increases up to 7 m/s, but begins to increase at higher wind speeds (not shown). This trend is consistent with previous NRCS measurements from TRMM PR [44] and GPM PR [45]. Although earlier studies have suggested that wind-direction sensitivity becomes

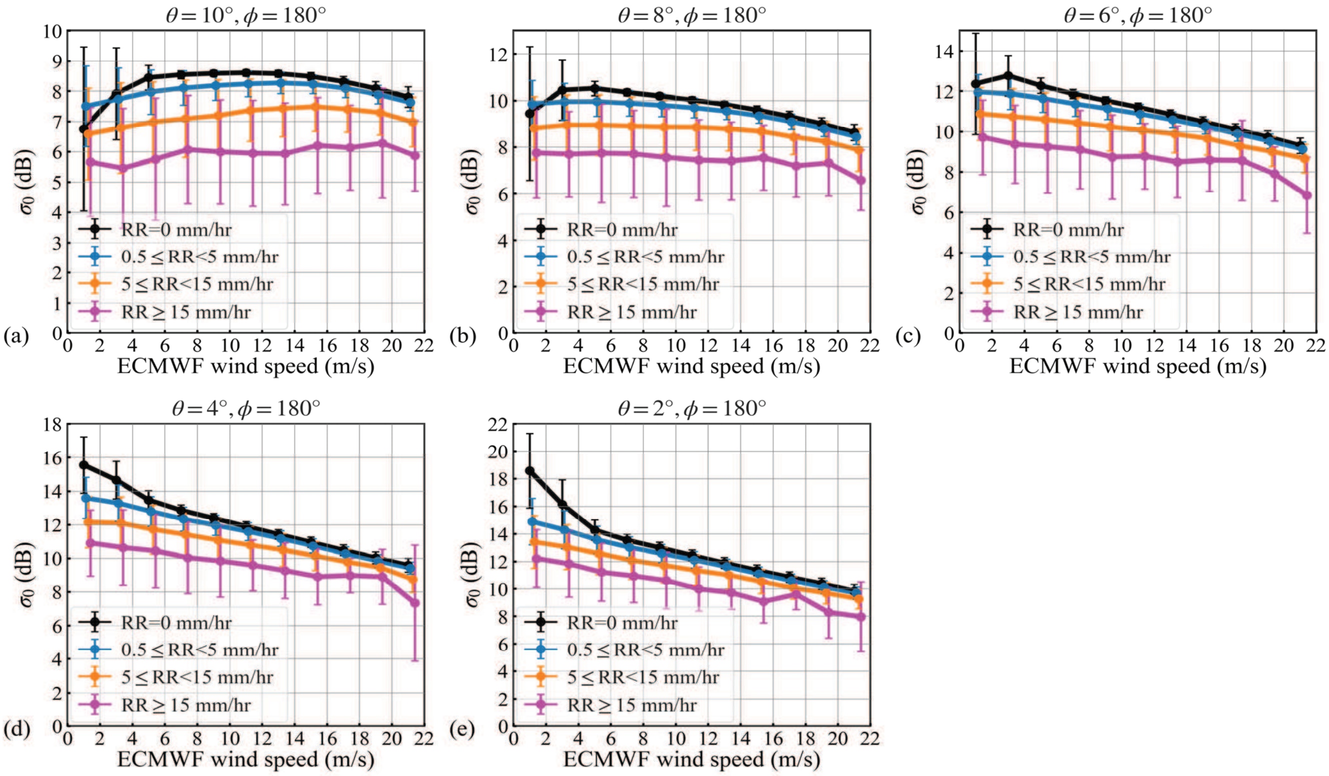

Fig. 5. Averaged SWIM NRCS at incidence angles of (a) 10°, (b) 8°, (c) 6°, (d) 4°, and (e) 2°, plotted as a function of ECMWF wind speeds under rain-free conditions (black lines) and for three rain rate categories: 0.5 ≤ RR <5 mm/h (blue), 5 ≤ RR <15 mm/h (orange), and RR ≥ 15 mm/h (magenta). Vertical bars represent the standard deviations within each 2 m/s wind speed bin. Rain rates are obtained from GPM and NEXRAD observations.

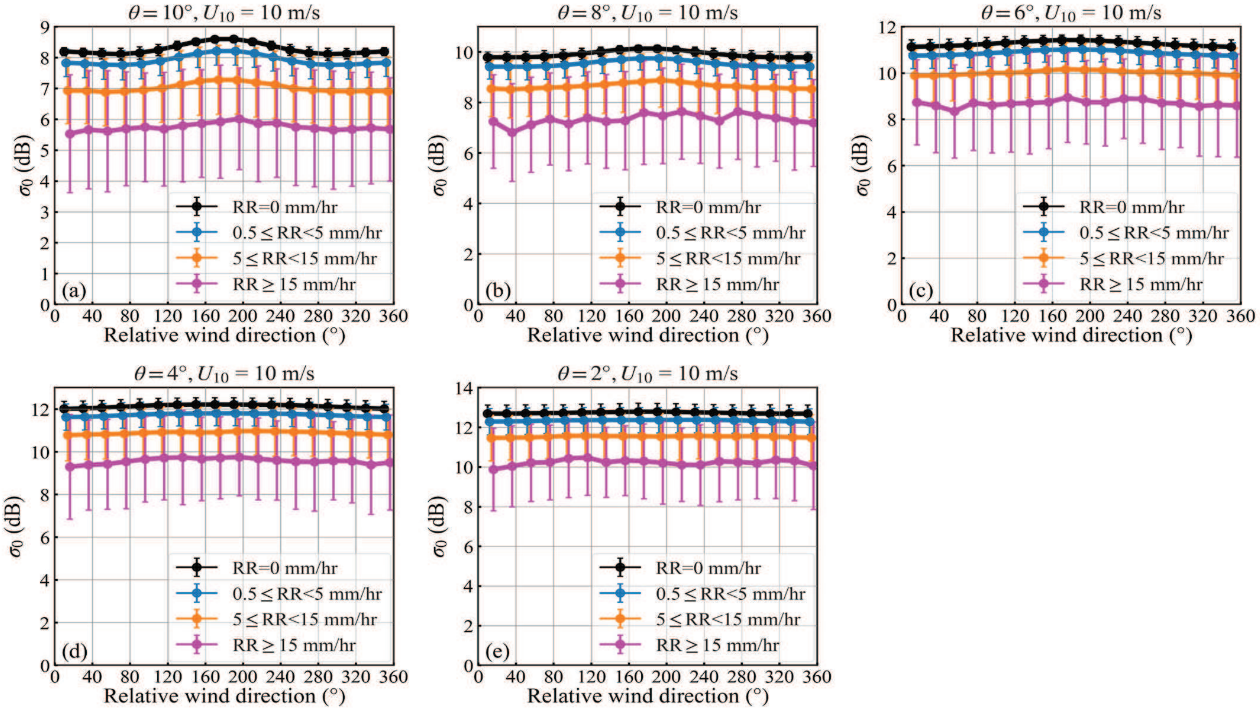

Fig. 6. Weighted averages of SWIM NRCS at incidence angles of (a) 10°, (b) 8°, (c) 6°, (d) 4°, and (e) 2°, plotted as a function of relative wind directions under rain-free conditions (black lines) and for three rain rate categories: 0.5 ≤ RR <5 mm/h (blue), 5 ≤ RR <15 mm/h (orange), and RR ≥ 15 mm/h (magenta). Vertical bars represent the standard deviations within each 20° relative wind direction bin. Rain rates are obtained from GPM and NEXRAD observations.

significant only at incidence angles exceeding approximately 6°, our results reveal a small but detectable azimuthal dependence even at lower incidence angles and low wind speeds. For example, at a wind speed of 3 m/s, the crosswind-

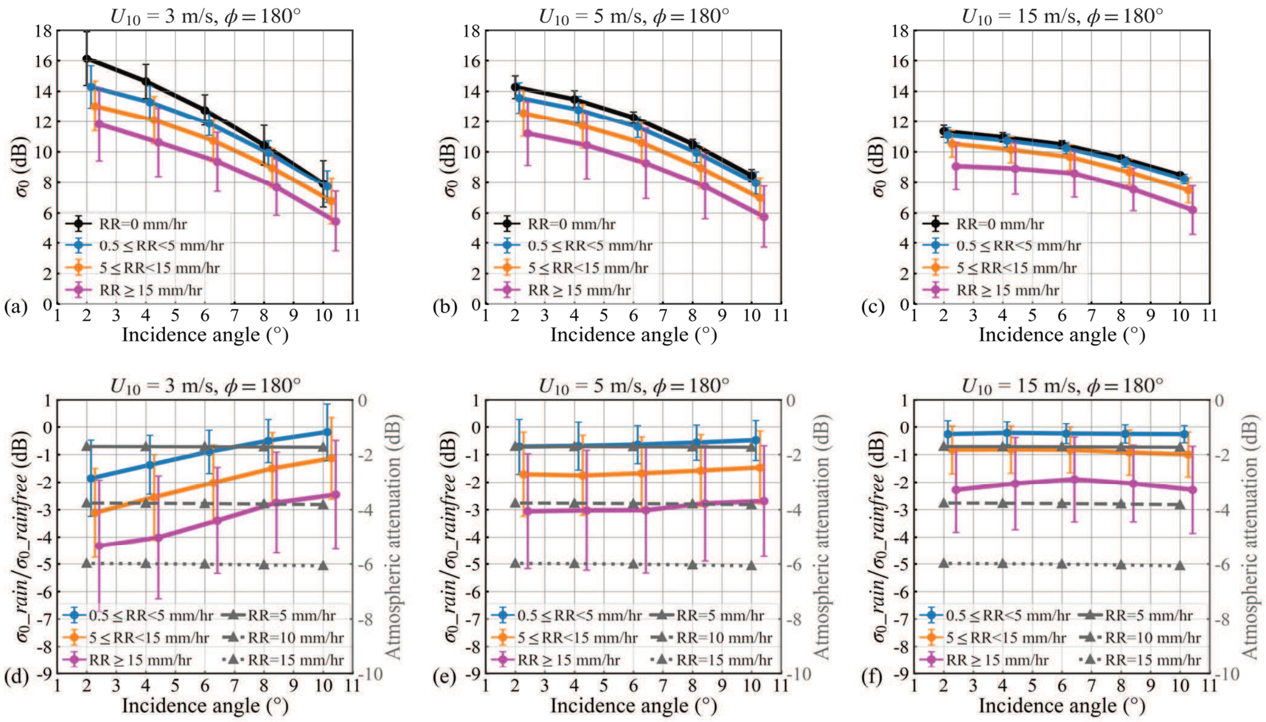

Fig. 7. Weighted averages of SWIM NRCS for wind speeds of (a) 3, (b) 5, and (c) 15 m/s, plotted as a function of incidence angle under rain-free conditions (black), and for three rain rate categories: 0.5 ≤ RR <5 mm/h (blue), 5 ≤ RR <15 mm/h (orange), and RR ≥ 15 mm/h (magenta). Vertical bars represent the standard deviations within each 2° incidence angle bin. (d)–(f) Corresponding ratios of NRCS under rainy and rain-free conditions. The gray line represents the estimated attenuation due to raindrops in the atmosphere, assuming a rain layer height of 1 km. Rain rates are obtained from GPM and NEXRAD observations.

to-downwind NRCS differences are 0.13 and 0.19 dB at incidence angles of 2° and 4°, respectively (not shown). As shown in Fig. 6, under light to moderate rain (0.5–5 mm/h), NRCS decreases by approximately 0.4 dB across all incidence angles. At higher rain rates, azimuthal variations become negligible. These observations confirm that using a fixed look direction (i.e., the downwind viewing in Fig. 5) provides a reliable basis for analyzing rain-induced NRCS changes, as directional dependencies are relatively minor compared to the reductions caused by rainfall, particularly for rain rates above 5 mm/h.

As discussed in the context of Fig. 5, the impact of rain on NRCS depends on the incidence angle. To further examine this relationship, Fig. 7(a)–(c) presents SWIM NRCS as a function of incidence angle in the downwind direction for three different wind speeds: 3, 5, and 15 m/s. The corresponding NRCS ratios between rainy and rain-free conditions are shown in Fig. 7(d)–(f). All incidence angle bins have a width of 2°. At all wind speeds and incidence angles, the mean NRCS ratio remains below 0 dB, confirming that rain consistently attenuates radar backscatter. The magnitude of this reduction can exceed 4 dB, particularly at low incidence angles, low wind speeds, and high rain rates, as observed in Fig. 7(a) and (d). In general, the influence of rain increases with rain rate across all wind speeds and incidence angles. At the low wind speed of 3 m/s, the NRCS reduction exhibits a clear dependence on incidence angle, with the largest decrease occurring at the smallest incidence angle. In contrast, for wind speeds of 5 m/s and above, the NRCS reduction becomes largely insensitive to incidence angle, indicating reduced dependence on beam geometry under stronger wind forcing.

To better understand the observed behavior, we assessed the effects of atmospheric attenuation and volume scattering caused by rain, following the methodology described in [31]. At near-nadir incidence angles, the contribution of volume scattering from raindrops was found to be at least 50 dB below typical NRCS values under rain-free conditions and can therefore be neglected. In contrast, atmospheric attenuation plays a more prominent role, primarily influenced by the rain rate and the vertical extent of the rain layer. Assuming a rain layer height of 1 km, the estimated attenuation is depicted by the gray line in Fig. 7(d)–(f), with values reaching approximately 1.7 and 6.0 dB for rain rates of 5 and 15 mm/h, respectively. Notably, the incidence angle exerts only a minor effect on attenuation within the SWIM near-nadir geometry, suggesting that the observed NRCS variations with incidence angle at low wind speeds are primarily attributable to surface effects rather than atmospheric ones. At low wind speeds, the negative slope of NRCS versus incidence angle becomes less steep as rain rate increases, which implies enhanced surface roughness under quasi-specular reflection conditions. However, based on Figs. 5–7, it remains challenging to quantitatively separate the effects of atmospheric attenuation from those of surface perturbations, as the actual rain layer depth, necessary for precise attenuation estimation, is unknown. To address this limitation, we introduce in Section IV a simplified model that enables the separation of these contributions.

To further illustrate the impact of rain on radar backscatter, we calculated the ratio of NRCS values under rainy and rain-free conditions, within bins of ±1° in incidence angle, ±1 m/s in wind speed, and ±20° in relative wind direction. The results, shown in Fig. 8, are plotted as a function of

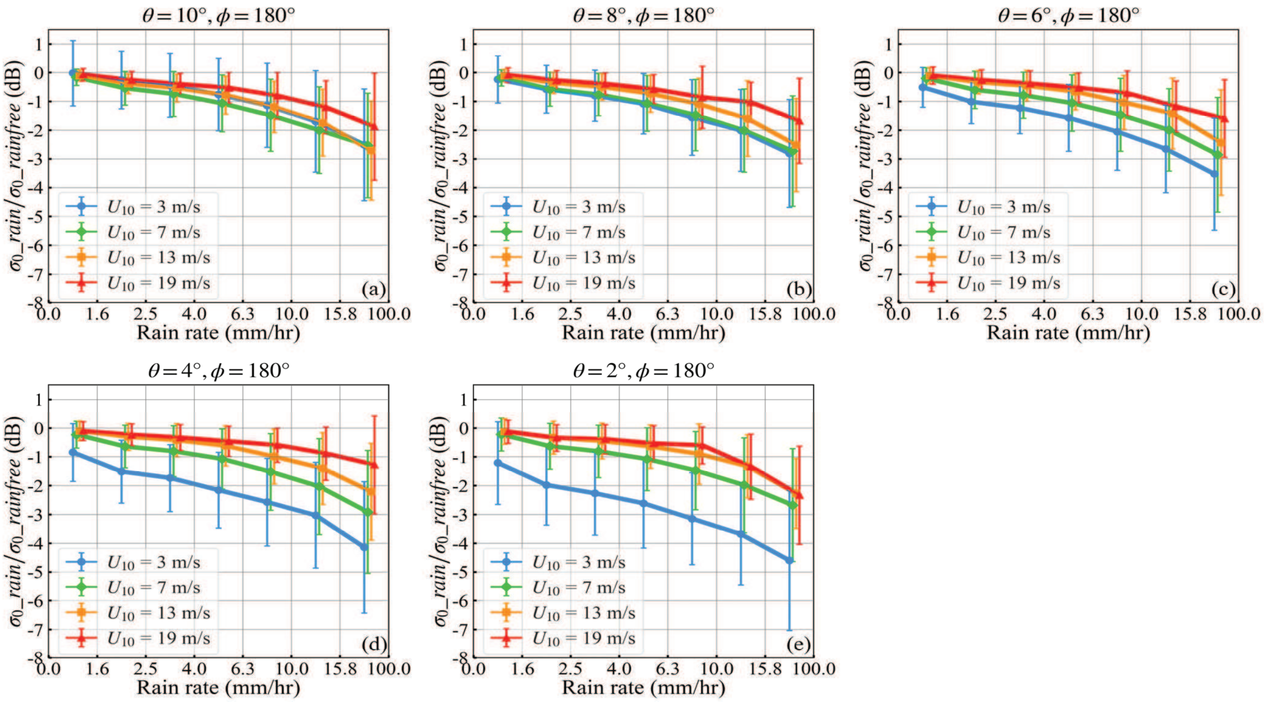

Fig. 8. Ratios of SWIM NRCS values under rainy and rain-free conditions at incidence angles of (a) 10°, (b) 8°, (c) 6°, (d) 4°, and (e) 2°, plotted as a function of rain rates. Results are shown for wind speeds of 3 m/s (blue), 7 m/s (green), 13 m/s (orange), and 19 m/s (red). Vertical bars represent the standard deviations. Rain rates are obtained from GPM and NEXRAD observations.

rain rate for four representative wind speeds: 3 m/s (blue), 7 m/s (green), 13 m/s (orange), and 19 m/s (red). This analysis provides a more detailed view of how rain affects NRCS across varying combinations of wind speed and incidence angle. For all incidence angles from 2° to 10° and all wind speeds, the mean NRCS ratio remains below 0 dB, confirming that rain consistently reduces radar backscatter as measured by SWIM. Moreover, the NRCS ratio decreases with increasing rain rate, indicating that the attenuation effect becomes more pronounced as rainfall intensifies. During weak rain events (up to 2.5 mm/h), NRCS reductions are generally less than −1 dB across all wind speeds and incidence angles, except at the smaller incidence angles of 2° and 4°, as shown in Fig. 8(d) and (e). Under these conditions, particularly in light wind regimes, NRCS reduction can reach up to −2 dB. In contrast, under heavy rain conditions (RR >15.8 mm/h), NRCS reductions become substantial across all wind speeds and incidence angles. The effect is most pronounced at lower incidence angles, where the NRCS decrease can reach up to −4.6 dB at 2°, as illustrated in Fig. 8(e). These results highlight the significant influence of rainfall on radar backscatter, especially at small incidence angles and during intense precipitation. The clear dependence on both rain rate and incidence angle emphasizes the importance of accounting for rain effects on NRCS measurements, particularly for ocean remote sensing applications using near-nadir radar observations.

The results under non-TC conditions clearly show that rainfall generally leads to a reduction in SWIM-measured NRCS. This attenuation is modulated by several factors, including rain rate, radar incidence angle, and wind speed. The impact of rain is most pronounced at lower incidence angles and under low wind conditions, where significant NRCS decreases are observed. In contrast, at higher wind speeds, the attenuation becomes less sensitive to incidence angle and less pronounced overall. The largest NRCS reductions is approximately 4.5 dB, occurs at a low incidence angle of 2°, high rain rate (>15 mm/h), and a low wind speed of 3 m/s. This notable decrease in NRCS results from a combination of atmospheric attenuation and rain-induced perturbations to the ocean surface. The relative reduction in NRCS strongly depends on wind speed at low incidence angles (≤ 6°), where wind-driven surface roughness predominantly affects radar backscatter. At higher wind speeds, wind-generated roughness dominates radar returns, diminishing the relative impact of rain. These findings highlight the complex interaction between wind, rain, and radar backscatter, with rain effects becoming detectable primarily under low wind conditions when rain-induced surface alterations are not overwhelmed by wind-driven roughness.

B. NRCS Signatures of Rain Under TC Conditions

To evaluate the impact of rain on SWIM NRCS under TC conditions, Section III-B1 presents an analysis of CFOSAT overpasses during two representative TC events in 2021. This case-based analysis is followed by a broader statistical investigation in Section III-B2, which examines global SWIM measurements collected during TCs over a three-year period (2021–2023).

1) Case Study—TC Surigae and Linda: We first analyze two TC cases from 2021: Surigae and Linda. TC Surigae formed over the tropical waters of the Northwest Pacific Ocean on April 11, 2021, and reached its peak intensity as

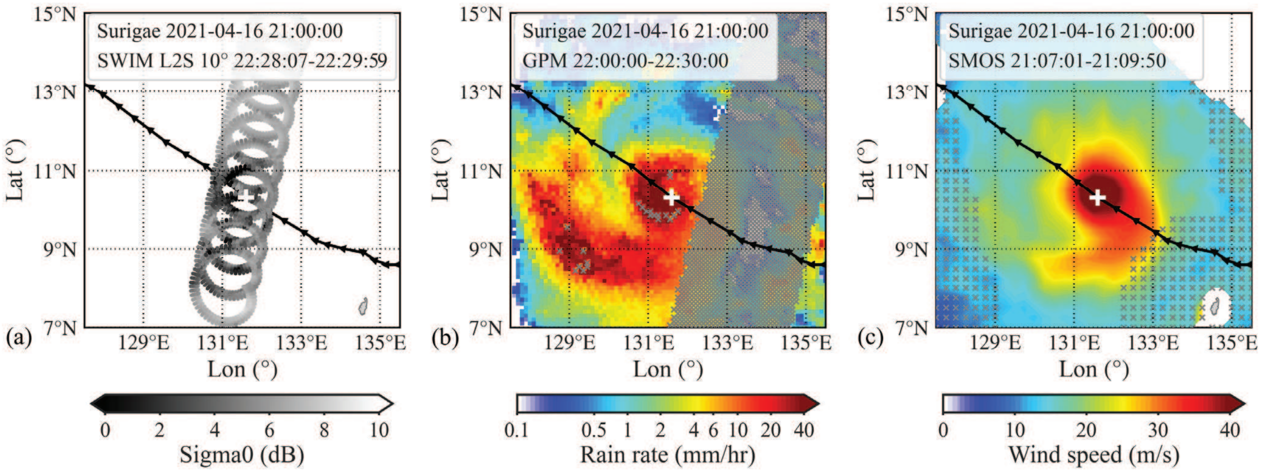

Fig. 9. CFOSAT overpass intersecting TC Surigae when it was a Category 4 storm on April 16, 2021. (a) SWIM L2S NRCS at a 10° incidence angle, acquired between 22:28:07 and 22:29:59 UTC; (b) GPM rain rates from 22:00 to 22:30 UTC; and (c) SMOS wind speeds from 21:07:01 to 21:09:50 UTC. The black arrow line represents the trajectory of Surigae, and the white plus sign denotes the cyclone's center at the time of the SWIM observation. In (b) and (c), gray crosses mark rain rates with a QI below 0.6 and SMOS wind speeds flagged as low quality.

a Category 5 storm, with wind speeds exceeding 87 m/s on April 17. During its mature stage, a descending CFOSAT pass intersected the storm's trajectory on April 16, capturing observations as Surigae moved northwestward, as shown in Fig. 9(a). The second case, TC Linda, was a long-lived system in the Northeast Pacific Ocean, forming on August 9, 2021, and persisting for over two weeks. For this analysis, a descending CFOSAT pass on August 16 was selected, corresponding to a period when Linda intensified to a Category 2 storm with maximum sustained winds of 48 m/s.

Fig. 9(a) shows SWIM L2S NRCS from the 10° incidence angle within TC Surigae on April 16, 2021, acquired during a descending pass from 22:28:07 to 22:29:59 UTC. The corresponding GPM rain rates, averaged over 22:00–22:30 UTC interval, are presented in Fig. 9(b), while SMOS wind speeds, acquired from 21:07:01 to 21:09:50 UTC, are shown in Fig. 9(c). In Fig. 9(b) and (c), gray crosses denote GPM rain rates with QI values below 0.6 and SMOS winds flagged as low quality (QL =2); these data are excluded from the broader statistical analysis in Section III-B2. For TC Surigae, only SMOS wind speeds were collocated with SWIM observations using the method described in Section II-E. In contrast, for TC Linda, both SMAP and SMOS wind products were available for collocation. However, the SMOS pass did not fully capture the cyclone's center and eyewall, and most SMOS wind speeds near the SWIM track were flagged as low quality. Consequently, despite a larger time offset, SMAP wind data are used for the Linda case, due to their better spatial coverage and higher data quality near the storm center.

As shown in Fig. 9(b), TC Surigae exhibits a pronounced asymmetry in its precipitation structure, with the maximum rain rate (49.5 mm/h) occurring to the left of the storm's moving direction. In contrast, the surface wind speeds display a relatively symmetrical pattern around the cyclone center, as shown in Fig. 9(c). The peak wind speed exceeds 44 m/s and is located to the right of the storm's trajectory. This value is approximately 19% lower than the equivalent 10-min mean wind speed reported by IBTrACS, after applying a gust factor conversion [46]. The spatial offset between the wind and rain maxima suggests a vertical tilt in the precipitation field, likely due to the sloped structure of the eyewall. Such misalignment is a common feature of intense TCs and highlights the importance of accounting for 3-D storm dynamics when interpreting satellite observations. Notably, areas of significantly reduced NRCS observed by SWIM closely follow the spiral rainbands of TC Surigae, as evident in the collocated GPM rain rate field. In contrast, SWIM observations farther from the rainbands generally exhibit higher NRCS values, consistent with rain-free conditions and minimal atmospheric attenuation.

A detailed view of a full antenna rotation during CFOSAT overpasses of TCs Surigae and Linda is presented in Fig. 10, with (a)–(f) corresponding to Surigae and (g)–(l) to Linda. The first and third rows display SWIM NRCS measurements at the 10° incidence angle, while the second and fourth rows show NRCS at 6°. For each case, the left column shows the NRCS overlaid with GPM rain rates, the middle column overlays NRCS with radiometer-derived wind speeds, and the right column presents NRCS–rain–wind triplets as a function of radar azimuth angle. During the first antenna rotation over TC Surigae (top row of Fig. 10), a clear attenuation in NRCS is observed as the SWIM footprint intersects the storm's rainbands. At an azimuth angle of 167°, the NRCS drops to 3.8 dB in a region with a rain rate of 10.8 mm/h and a wind speed of 30.9 m/s. In contrast, in the northeast and northwest sectors, where rain rates are below 1 mm/h, the NRCS remains around 7.2 dB, indicating a rain-induced NRCS attenuation of more than 3 dB. At the 6° incidence angle (second row), a similar attenuation pattern is observed, though the magnitude of reduction is slightly smaller (~3 dB), occurring under comparable conditions: a rain rate of 9.5 mm/h and a wind speed of near 30 m/s. For TC Linda, as shown in Fig. 10(g)–(i), the SWIM track intersects the cyclone's eyewall, resulting in two distinct NRCS drops at the 10° incidence angle. The second drop, occurring at an azimuth angle of 101°, corresponds to a rain rate of 11.8 mm/h and a wind speed of 33.6 m/s, where the NRCS decreases by more than 6 dB. As Linda approaches

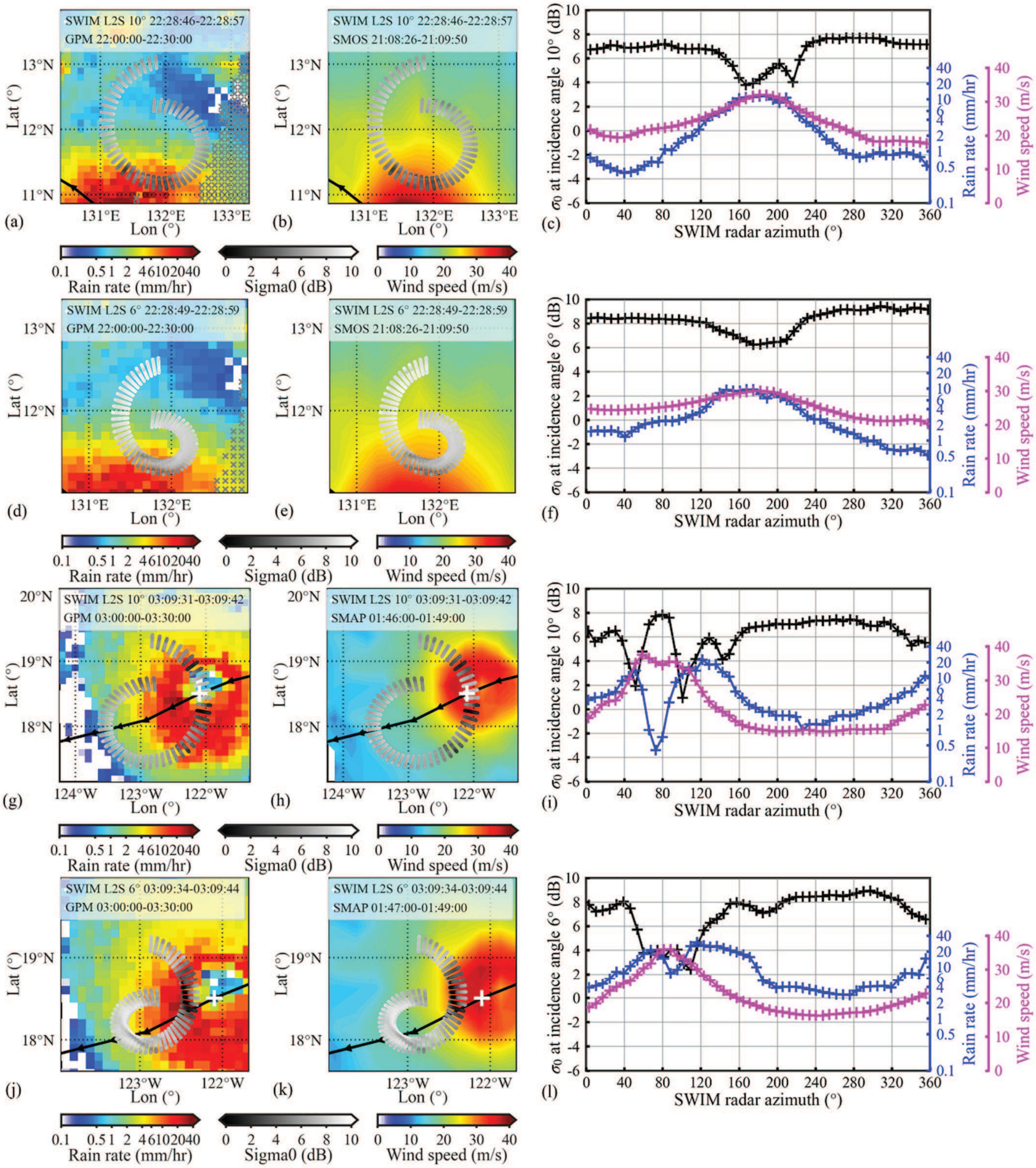

Fig. 10. SWIM NRCS measurements during CFOSAT overpass of TCs (a)–(f) Surigae and (g)–(l) Linda. Panels in the first and third rows show NRCS at a 10° incidence angle, while those in the second and fourth rows correspond to a 6° incidence angle. In each group, the first column displays GPM rain rates (color shading) overlaid with the SWIM footprint, where grayscale indicates NRCS values along the track. The second column presents SMOS or SMAP wind speeds. The third column plots mean values of NRCS (black), GPM rain rate (blue), and SMOS and/or SMAP wind speed (magenta) as functions of SWIM radar azimuth angle.

peak intensity, it becomes evident that variations in wind speed have a limited effect on the NRCS at the 10° incidence angle and only a moderate effect at 6°. In contrast, rain rates exceed approximately 10 mm/h lead to significant attenuation at both incidence angles.

The variations in NRCS and rain rates are generally well correlated. However, discrepancies in azimuth alignment occasionally occur between regions of heavy rainfall and adjacent areas of pronounced radar signal attenuation. For example, in the case of TC Linda, as shown in Fig. 10(i), the minimum NRCS occurs at an azimuth angle of 101°, where the rain rate is approximately 12 mm/h, while the maximum rain rate of 15.8 mm/h is observed farther away, at 108°. A similar spatial offset is also observed in Fig. 10(l). These

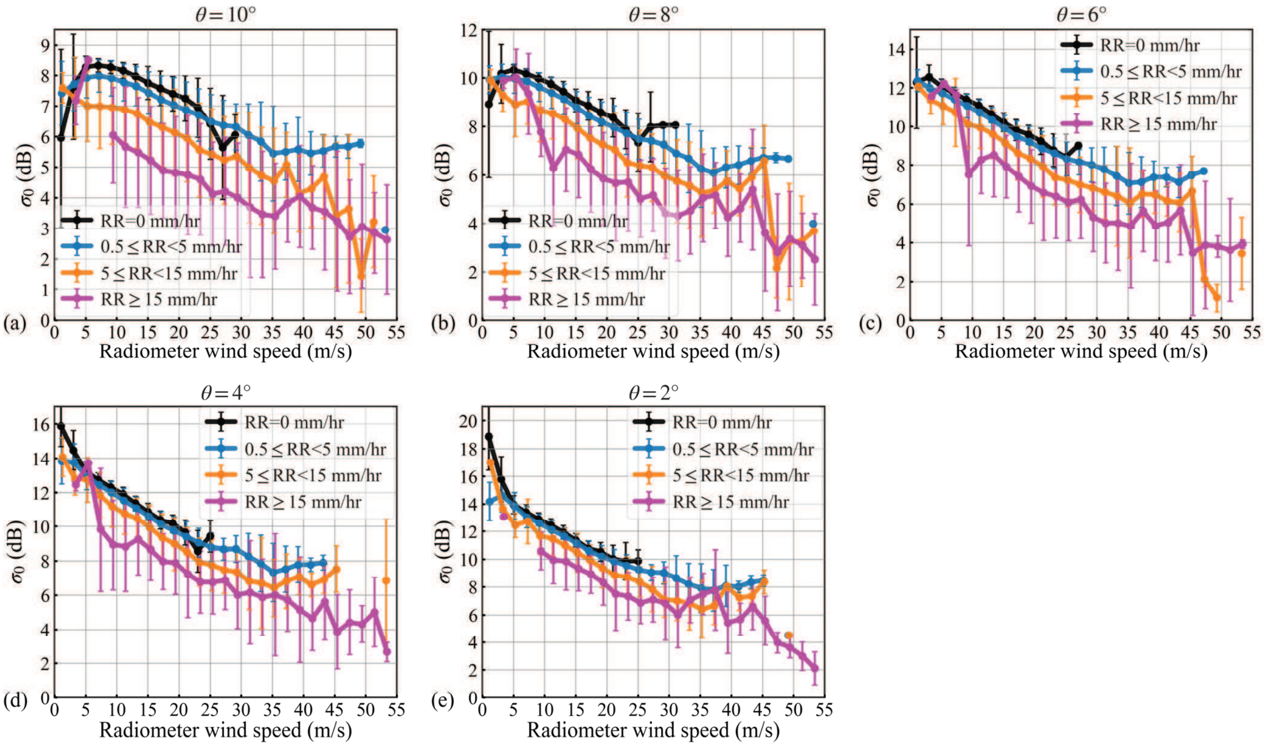

Fig. 11. SWIM NRCS at incidence angles of (a) 10°, (b) 8°, (c) 6°, (d) 4°, and (e) 2°, plotted as a function of wind speed under rain-free conditions (black lines) and for three rain rate categories: 0.5 ≤ RR <5 mm/h (blue), 5 ≤ RR <15 mm/h (orange), and RR ≥ 15 mm/h (magenta). Vertical bars represent the standard deviations within each 2 m/s wind speed bin. Rain rates are obtained from GPM and NEXRAD observations.

misalignments may result from uncertainties in the spatiotemporal collocation process or from rapid changes in convective activity during the time interval between the observations. Notably, within a 3-h window before and after the CFOSAT overpass, TC Linda's maximum sustained wind speed fluctuated from 48.8 to 46.3 m/s, indicating a 5% variation in storm intensity. This further supports the possibility of evolving convective structures during the observation period, which may contribute to the observed offsets.

2) Statistics Study—Global TCs: To further investigate the behavior of NRCS under rainfall and high wind conditions, SWIM observations were analyzed during CFOSAT overpasses of numerous TCs across the global oceans. Fig. 11 displays the off-nadir radar backscatter as a function of wind speed, with wind data derived from SMOS and/or SMAP measurements. The data are grouped into 2 m/s wind speed bins, and NRCS values within each bin are averaged using weighted means. The classification of rain rates follows the same three categories defined in Section III-A2.

A comparison of radar backscatter under rain-free conditions (RR =0 mm/h) shows a general decrease in NRCS with increasing rain rate. Since no NRCS measurements are available for wind speed above approximately 27 m/s under rain-free conditions, and given that the results for winds below 27 m/s are nearly identical between RR = 0 and 0.5 ≤ RR <5 mm/h, the light to moderate rain category (0.5 ≤ RR <5 mm/h) is used here as a proxy for rain-free conditions. For near-nadir incidence angles, NRCS decreases by approximately 2–3 dB when the rain rate exceeds 15 mm/h and wind speeds range from about 13 to 33–35 m/s. At wind speeds above roughly 35 m/s, NRCS values for 0.5 ≤ RR <5 mm/h category tend to saturate, whereas those for RR ≥ 15 mm/h continue to decrease. This behavior suggests that significant attenuation may occur under heavy rainfall and TC-force wind conditions.

Radar backscatter at low incidence angles has previously been investigated using TRMM and GPM PR observations within TCs under rain-free and light to moderate rainfall conditions (i.e., RR <5 mm/h) [47], [48]. The SWIM-measured NRCS values presented in Fig. 11 are generally consistent with these earlier findings, showing discrepancies of approximately 1–2 dB for wind speeds between 6 and 32 m/s. At higher wind speeds (above approximately 35 m/s), our results further support the observed trend that NRCS becomes increasing insensitive to wind speed. As noted by Li et al. [47], this behavior under extreme wind conditions is likely associated with changes in the drag coefficient, which may saturate or even decrease. Such changes can lead to a relatively smoother ocean surface [49], thereby limiting the decrease in NRCS at near-nadir incidence angles as wind speed increases.

IV. DISCUSSION

A. *Impact of Rain on Geophysical Parameters*

The impact of rain on SWIM NRCS is investigated using two datasets constructed under non-TC and TC conditions. For the non-TC dataset, surface wind speeds are derived from the ECMWF reanalysis data. In contrast, the TC dataset utilizes wind speeds from microwave radiometer products, which provide more reliable estimates under extreme wind conditions. Rain rates for both datasets are obtained from GPM and NEXRAD precipitation products. A comparison between the two datasets is feasible at moderate to high wind speeds (up to about 21 m/s), where differences in NRCS behavior due to rain are more distinguishable. To strengthen this comparison, NRCS and ECMWF wind data collected during TC events are also included in the analysis.

In the absence of rain, the maximum differences in near-nadir NRCS are less than 0.7 dB when comparing TC cases with radiometer winds to either non-TC cases or TC cases using ECMWF winds. The most notable discrepancies occur at wind speeds below 10–12 m/s and rain rates exceeding 5 mm/h, partially supporting the notion that L-band radiometer wind estimates are less reliable under low wind speed conditions. Moreover, such conditions are rare in our dataset, representing only 1.25% of TC cases with radiometer wind data.

Under rainy conditions, a comparison between the two datasets within the wind speed range of 13–20 m/s shows that the NRCS reduction is more pronounced in the TC dataset than in the non-TC dataset for comparable rain rates. This difference is likely due to the greater vertical extent of the rain layer in TC environments. Specifically, in TCs, the rain layer may extend up to approximately 5 km (reaching the freezing level), whereas under non-TC conditions, a typical depth of about 1 km is more common, as reflected in the attenuation curves shown in Fig. 7.

Our results show that the primary effect of rain is to attenuate NRCS measured at near-nadir incidence angles. At low wind speeds, the NRCS reduction varies with incidence angle, suggesting that atmospheric attenuation alone does not fully account for the observed behavior (see Fig. 7). Under these conditions, the surface mean square slope appears to increase, likely due to the formation of ring waves caused by impinging raindrops, which further reduces NRCS. At moderate wind speeds, this incidence angle dependence disappears, possibly because rain-induced surface roughness becomes negligible compared to wind-driven roughness. Interestingly, the anticipated wave-damping effect is not observed, likely because rain attenuation dominates and masks the NRCS increase that damping might cause. Although previous studies have identified ring wave generation as the primary rain-induced mechanism affecting radar backscatter, our analysis of the non-TC dataset does not fully support this conclusion. While the effect may still be present, it appears largely obscured by concurrent atmospheric attenuation.

As wind speeds reach storm-level magnitudes, the ocean surface becomes increasingly affected by wave breaking, whitecaps, and foam. Under these conditions, it is generally accepted that surface roughness saturates or even decreases with further wind speed increases due to energy saturation in the wave spectrum [50]. However, our NRCS analysis under heavy rainfall (RR ≥ 15 mm/h) and severe wind conditions (above approximately 35–40 m/s) reveals a continued decline in NRCS with increasing wind speed (see Fig. 11). This behavior suggests that raindrops may further enhance surface roughness, thereby contributing to the observed NRCS reduction. Under TC conditions, rain-generated ring waves are expected to be suppressed by intense wind forcing. However, secondary splash products generated by raindrops, such as stalks, may still increase surface roughness. This additional roughness, particularly under extreme wind and rain conditions, could modulate radar backscatter and may partially explain the persistent NRCS decline observed in our dataset.

The innovative SWIM instrument utilizes a near-nadir scanning beam geometry to measure the directional wave spectrum. By conducting spectral analysis of NRCS fluctuations within each footprint along the radar look direction, the observed modulation spectrum is transformed into the wave slope spectrum. Notably, SWIM is specially designed to capture surface waves with wavelengths ranging from 70 to 500 m, providing valuable insights into wave dynamics across diverse oceanic conditions.

As previously discussed, rainfall over the ocean can significantly affect SWIM NRCS measurements. In our earlier study [3], we investigated the impact of rain on the surface wave spectrum measured by SWIM during TC Sam (2021). A comparison between wave spectra derived from SWIM and situ instruments demonstrated good agreement, even under rainy conditions. Furthermore, analysis of SWIM radar's postprocessing chain indicates that rainfall primarily affects the modulation spectrum at longer wavelengths (greater than 1 km). This finding suggests that the wave spectrum retrieved by SWIM measurements remains reliable, even in the presence of heavy rainfall.

As previously noted, NRCS at small incidence angles exhibits a strong correlation with wind speed (see Fig. 4), along with a modest but significant sensitivity to wind direction. This indicates that SWIM has the potential to retrieve wind information from NRCS measurements, provided that the effects of rain contamination can be effectively quantified and corrected. As previously shown by Ren et al. [51], wind speed retrieved from SWIM data at incidence angles below 7.5° shows good agreement with measurements from the CFOSAT scatterometer. In their study, a rain flag derived from nadir-viewing observations was used to exclude rain-contaminated data. Nevertheless, further development is needed to improve rain correction techniques and enhance the accuracy of wind retrievals from SWIM measurements.

B. Separation of Atmospheric Attenuation and Surface Effect

To evaluate the various effects of rain on radar backscatter, we use a simplified model that characterizes the rain-modified NRCS by incorporating both atmospheric attenuation and rain-induced changes in surface roughness. The expression for this model is given as follows:

$$\sigma_{0m} = \alpha_{\text{atm}} \left[(\sigma_{0w} - \sigma_{0\text{sr}}) + \sigma_{0v} \right]. \tag{1}$$

In this formulation, the rain-affected NRCS, denoted as σ_{0m}, is modeled as a combination of several components: σ_{0w}, the surface backscatter due to wind alone; $\sigma_{0\text{sr}}$, the additional surface backscatter generated by raindrops; α_{atm}, the two-way attenuation caused by atmospheric rain; and σ_{0v}, the volume scattering contribution from raindrops in the atmosphere.

In (1), the negative sign preceding $\sigma_{0\text{sr}}$ indicates that, when $\sigma_{0\text{sr}}$ is considered positive, the net effect of rain is a reduction in the total backscatter due to modifications in surface roughness. This implies that rain-induced surface effects tend to increase the surface roughness compared to non-rainy conditions; In particular, features such as ring waves and splashes generated by raindrops contribute more significantly to the roughness than potential smoothing effects associated with near-surface turbulence.

The term σ_{0v} in (1) represents volume scattering from atmospheric raindrops, can be considered negligible. Based on the formulation proposed by Tournadre and Quilfen [31], we estimate that at small incidence angles (2°–10°), σ_{0v} ranges from −63 to −49 dB for rain rates between 1 and 15 mm/h, assuming a rain layer height of 1 km. These values are approximately 58–76 dB lower than the typical magnitude of σ_{0w}, confirming that volume scattering has a negligible impact on the total measured backscatter.

We define the ratio of σ_{0m} at the 10° incidence angle, denoted as σ_{0m_10}, to the corresponding σ_{0m} at any other SWIM incidence angle i (i.e., 2°, 4°, 6°, or 8°), denoted as σ_{0m_i}

$$Q_{10/i} = \frac{\sigma_{0m\_10}}{\sigma_{0m\_i}}. \tag{2a}$$

Since σ_{0v} can be considered negligible at all small incidence angles, for a given wind speed and rain rate, the ratio $Q_{10/i}$ can be approximated as

$$Q_{10/i} \sim \frac{\sigma_{0w\_10} - \sigma_{0\mathrm{sr}\_10}}{\sigma_{0w\_i} - \sigma_{0\mathrm{sr}\_i}}. \tag{2b}$$

Since backscatter at a 10° incidence angle is largely insensitive to variations in surface roughness at least for wind speeds between 3 and 14 m/s (see Fig. 4), we assume that rain-induced changes in surface roughness does not significantly affect the NRCS at 10°. Accordingly, we set $\sigma_{0\mathrm{sr}\_10} = 0$ in our formulation. We acknowledge that this is a simplification and will revisit its validity when analyzing the estimated values of $\sigma_{0\mathrm{sr}\_i}$ at smaller incidence angles. Based on (2), $\sigma_{0\mathrm{sr}\_i}$ is expressed as

$$\sigma_{0\mathrm{sr}\_i} = \sigma_{0w\_i} - \frac{\sigma_{0w\_10}}{Q_{10/i}}. \tag{3}$$

Assuming that σ_{0w_i} and σ_{0w_10} are prescribed using our results under rain-free conditions (see Fig. 4), the term $\sigma_{0\mathrm{sr}\_i}$ can be estimated from (3). The corresponding results for the non-TC cases are shown in Fig. 12, for SWIM incidence angles of 2°, 4°, 6°, and 8°, as a function of rain rate and for different wind speeds (3, 7, 11, and 13 m/s). It is noteworthy that both positive and negative values of $\sigma_{0\mathrm{sr}\_i}$ are observed in Fig. 12. According to (1), a positive value of $\sigma_{0\mathrm{sr}\_i}$ implies that rain reduces the backscatter compared to rain-free conditions. However, the relationship is not straightforward, and it remains unclear whether rain consistently decreases or increases the NRCS. In cases where the estimated $\sigma_{0\mathrm{sr}\_i}$ is negative, which is physically implausible, this may suggest that the sign of the $\sigma_{0\mathrm{sr}\_i}$ term in (1) should be reversed. That is, under certain conditions, rain may enhance the NRCS compared to rain-free conditions.

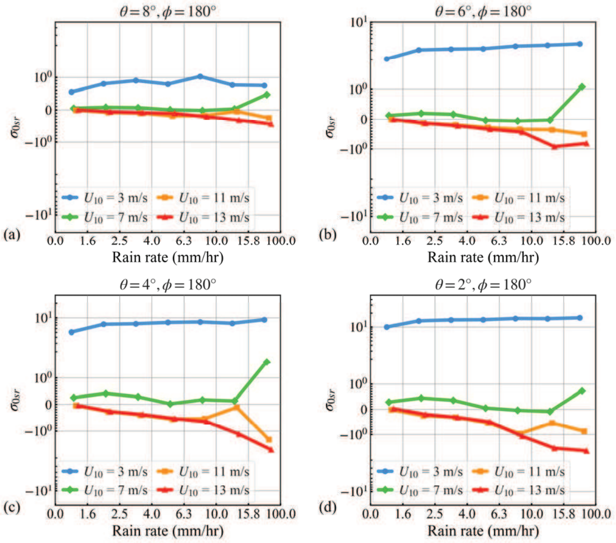

Fig. 12. Estimated rain-induced surface backscatter $\sigma_{0\mathrm{sr}}$ at incidence angle of (a) 8°, (b) 6°, (c) 4°, and (d) 2°, plotted as a function of rain rate. Results are derived from the non-TC dataset for wind speeds of 3 m/s (blue), 7 m/s (green), 11 m/s (orange), and 13 m/s (red). Rain rates are obtained from GPM and NEXRAD observations.

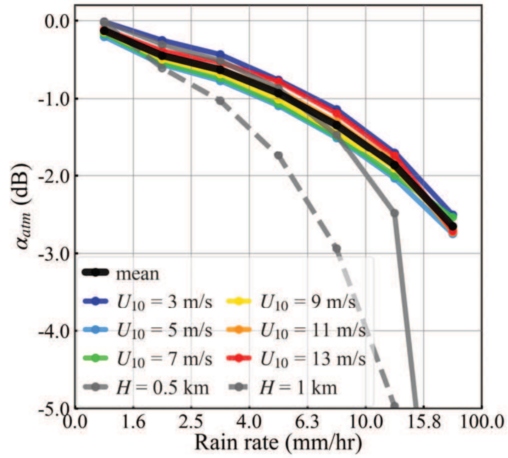

Fig. 13. Estimated atmospheric attenuation α_{atm} as a function of rain rate, derived from the non-TC dataset for wind speeds of 3 m/s (dark blue), 5 m/s (blue), 7 m/s (green), 9 m/s (gold), 11 m/s (orange), and 13 m/s (red). The black line represents the mean attenuation across wind speeds from 3 to 13 m/s. Gray lines denote the estimates by Tournadre and Quilfen [31], assuming rain layer heights of 0.5 km (solid line) and 1 km (dashed line). Rain rates are obtained from GPM and NEXRAD observations.

With the adopted sign convention, Fig. 12 shows that when wind speeds are below 7 m/s, the overall surface effect of rain is either neutral or leads to a reduction in backscatter compared to rain-free conditions. This suggests that, at incidence angles between 2° and 8°, where the radar backscatter is predominantly quasi-specular, rain tends to increase surface roughness. In this low wind regime, the contributions from ring waves and splashes generated by raindrops appear to dominate over damping effects on short gravity-capillary waves. Furthermore, Fig. 12 indicates that this surface roughening effect becomes more pronounced as wind speed decreases, with the largest impact observed at a wind speed of 3 m/s and an incidence angle of 2°. Neglecting the atmospheric effect and using σ_{0w} values from Fig. 4, we estimate that this corresponds to a relative variation of approximately −2.1 dB in NRCS compared to rain-free conditions.

In contrast, at wind speeds above 7 m/s, the overall surface effect of rain is either neutral or results in a slight increase

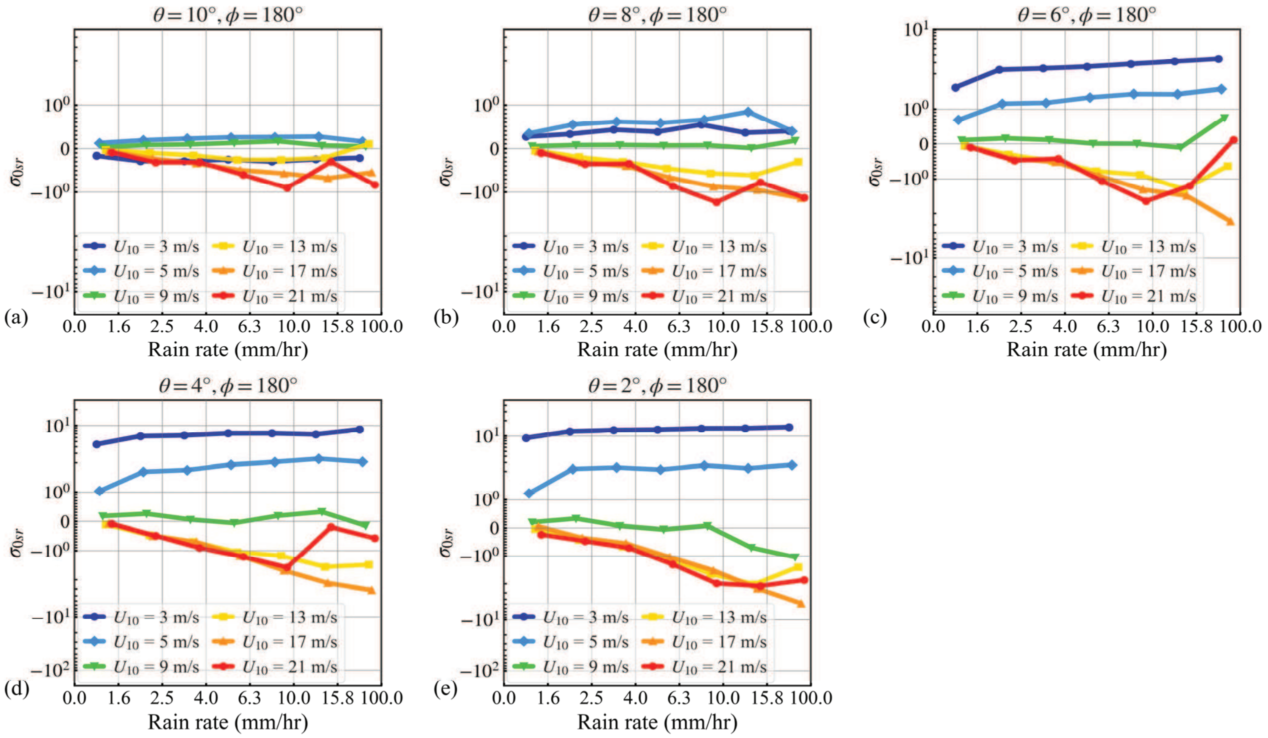

Fig. 14. Recalculated rain-induced surface backscatter σ_{0sr} (in m^2) at incidence angles of (a) 10°, (b) 8°, (c) 6°, (d) 4°, and (e) 2°, plotted as a function of rain rate. Results are derived from the non-TC dataset for wind speeds of 3 m/s (dark blue), 5 m/s (blue), 9 m/s (green), 13 m/s (gold), 17 m/s (orange), and 21 m/s (red). Rain rates are obtained from GPM and NEXRAD observations.

in backscatter compared to rain-free conditions. Under these conditions, rain appears to smooth the ocean surface, likely due to the dominant damping of short surface waves by raindrops. As shown in Fig. 12, this smoothing effect becomes more pronounced with increasing rain rate and decreases with increasing incidence angle. These observations are consistent with our earlier conclusion that, under moderate wind conditions, rain-induced wave damping is the dominant mechanism affecting the surface roughness. The maximum value observed at 4° incidence angle for a 13 m/s wind speed corresponds to a modest NRCS increase of approximately 0.5 dB. Thus, based on this straightforward analysis, we conclude that under low wind conditions (below 7 m/s), the perturbation of near-nadir backscatter by rain is primarily caused by the generation of ring waves and splashes. In contrast, at moderate wind speeds (≥ 7 m/s), rain-induced wave damping either offsets other surface roughness-enhancing effects or becomes the dominant mechanism affecting the radar backscatter signal. Based on this dataset, our evaluation of rain's impact on NRCS is limited to wind speeds between 3 and 13 m/s, due to the assumption that backscatter at a 10° incidence angle is insensitive to variations in surface roughness. We subsequently propose a method to extend this estimation to higher wind speeds.

Since σ_{0sr} at incidence angles between 2° and 8° have been estimated, we now return to (1) to estimate the atmospheric attenuation factor α_{atm}, while continuing to assume that σ_{0v} is negligible across all near-nadir incidence angles. This approach provides five independent estimates of α_{atm}, which exhibit minimal variation among them. The results at the 10° incidence angle are shown in Fig. 13. As illustrated, α_{atm} is largely independent of wind speed and depends primarily on rain rate, consistent with the lack of correlation between rain and wind. The estimated attenuation ranges from a fraction of a decibel at low rain rates (less than 1.6 mm/h) to approximately 2.8 dB for rain rates between 15.8 and 100 mm/h. These results agree well with those reported by Tournadre and Quilfen [31], assuming a rain layer height of 0.5 km and rain rates below 10 mm/h.

Assuming that the mean value of α_{atm}, as derived above, is independent of wind speed and incidence angle, we now recalculate σ_{0sr} for higher wind speeds using (1). This calculation uses the mean α_{atm} corresponding to different rain rates, along with the reference rain-free backscatter σ_{0w}, while continuing to assume that σ_{0v} is negligible. The results, shown in Fig. 14, depict σ_{0sr} as a function of rain rate for various wind speeds. For wind speeds between 3 and 13 m/s, the recalculated σ_{0sr} values align well with those previously presented in Fig. 12. Notably, at an incidence angle of 10°, σ_{0sr} remains close to zero for wind speed below 13 m/s, which a posteriori supports the assumption made earlier in generating Figs. 12 and 13. This consistency reinforces the validity of our simplified approach. For wind speeds exceeding 13 m/s, σ_{0sr} becomes negative across all incidence angles, indicating an increase in backscatter compared to rain-free conditions. This enhancement is attributed to the dominant role of rain-induced wave damping, which tends to smooth the ocean surface. The magnitude of this effect generally increases with increasing rain rate, although significant fluctuations occur at a wind speed of 21 m/s for rain rates above 10 mm/h.

Neglecting atmospheric attenuation, the largest surface effect (about 4.8 m^2) observed at 2° incidence angle under heavy rain corresponds to an increase of approximately 1.4 dB in NRCS compared to rain-free conditions.

In this section, we applied a simplified modeling approach leveraging the differing sensitivities of radar backscatter at small incidence angles (2°–8°) compared to 10°. By assuming that volume scattering by atmospheric droplets is negligible at small incidence angles, we estimate rain-induced perturbations to NRCS compared to rain-free conditions across various rain rates and wind speeds, and derive corresponding estimates of the atmospheric attenuation coefficient. The main finding is that the impact of rain on NRCS differs between low and moderate-to-high wind regimes. Under low wind conditions, rain-induced ring waves and/or splashes enhance surface roughness, reducing NRCS by up to 2 dB beyond atmospheric attenuation effects. In contrast, under moderate to high wind conditions, wave damping dominates, smoothing the surface and increasing in NRCS by up to 1.4 dB, which may partially compensate the impact of signal attenuation caused by the atmospheric raindrops. This increase correlates positively with rain rate and remains relatively consistent for wind speed above 13 m/s. A wind speed near 7 m/s appear to mark a transition between decreasing and increasing NRCS with rain. Applying this method to the TC dataset yields surface effect estimates (not shown) for moderate to high wind speeds (11–19 m/s) broadly consistent with those in Figs. 12 and 14, supporting the robustness of our approach. For wind speeds exceeding 20 m/s, the lack of rain-free observations limits the applicability of this method.

It is important to address that these results were derived using a simplified modeling framework that relies on the differing NRCS sensitivities to surface roughness at 10° and at smaller incidence angles, without requiring estimates of atmospheric attenuation. As an alternative approach, rain attenuation could be independently estimated from GPM data and incorporated into (1) to more explicitly separate surface and atmospheric contributions of rain to the observed NRCS. This validation is the subject of ongoing research and will be addressed in a forthcoming study.

V. CONCLUSION

Collocated CFOSAT SWIM observations with GPM and NEXRAD rain rate data have provided valuable insights into the impact of rain on Ku-band radar backscatter at near-nadir incidence angles. The analysis reveals that the NRCS under rainy conditions exhibits distinct and significant variations depending on incidence angle, rain rate, wind speed, and sea state. These findings highlight the complex interplay among atmospheric and oceanic factors affecting radar backscatter, especially in the presence of precipitation. They also emphasize the necessity of incorporating these factors into the development of robust remote sensing algorithms and applications.

Under non-TC conditions, the primary impact of rain on Ku-band radar backscatter is a reduction and a suppression of azimuthal variations, with attenuation effects becoming increasingly significant at higher rain rates. At low to moderate rain rates ($0.5 \leq \text{RR} < 5$ mm/h), NRCS attenuation is generally limited to a fraction of a decibel when wind speeds exceed 5 m/s. However, under heavy rain conditions ($\text{RR} \geq 15$ mm/h), attenuation can reach magnitudes of 3–5 dB, indicating a significant impact on radar backscatter. These findings highlight the critical importance of accounting for rain rate when interpreting radar measurements to ensure accurate retrievals of surface and atmospheric parameters. The attenuation effect tends to diminish with increasing wind speed, especially at the smallest incidence angles. At low wind speeds, NRCS reduction exhibits a strong dependence on incidence angle, but this dependence becomes negligible for wind speeds above 5 m/s. This differential behavior was leveraged to separate atmospheric attenuation and surface contributions of the rain impact using a simplified model that assumes NRCS at 10° is unaffected by surface effects. The analysis suggests that rain may increase roughness at wind speeds below 7 m/s but suppress it at higher wind speeds. This transition is attributed to different rain-induced mechanisms: splashes and ring wave generation dominate at low wind speeds, while wave damping becomes more significant at moderate to high wind speeds. Although surface effects are relatively minor compared to atmospheric attenuation, reaching approximately −2.1 and 1.4 dB in two wind regimes, they provide important insight into the variation of NRCS with rain across different incidence angles and wind speeds. Further research is needed to improve the characterization of the rain layer and associated atmospheric attenuation, thereby enhancing the accuracy of SWIM observations in rainy environments.

Surface wind data from the SMOS and SMAP radiometers were used to investigate the behavior of NRCS under rainy conditions during TCs. Overall, rain tends to reduce radar backscatter, with the degree of attenuation increasing as the rain rate increases. Compared to measurements obtained under light to moderate rain conditions ($0.5 \leq \text{RR} < 5$ mm/h), NRCS is attenuated by approximately 2–3 dB when rain rates exceed 15 mm/h and wind speeds range from 13 to around 33–35 m/s. This highlights the combined and compounding effects of both rain and wind on radar backscatter, especially under intense rain conditions. As rain rate and wind speed increase, attenuation becomes more pronounced, highlighting the need to account for these factors when interpreting radar measurements in TCs and other rain-affected environments. Within the wind speed range where radiometer wind estimates are most reliable (13–20 m/s), NRCS reduction under moderate to heavy rain ($\text{RR} > 5$ mm/h) in TC conditions are approximately 1 dB greater than those observed in non-TC environments. This discrepancy is likely due to deeper rain layer in TCs at comparable rain rates, resulting in greater atmospheric attenuation. As the wind speeds exceed approximately 35 m/s, NRCS under light to moderate rain rates tends to saturate, whereas under heavy rain, NRCS continues to decrease with increasing wind speed. This behavior suggests that, at extreme wind intensities, heavy rain exerts a more significant and persistent impact on radar backscatter, which must be considered in remote sensing applications targeting high-impact weather events.

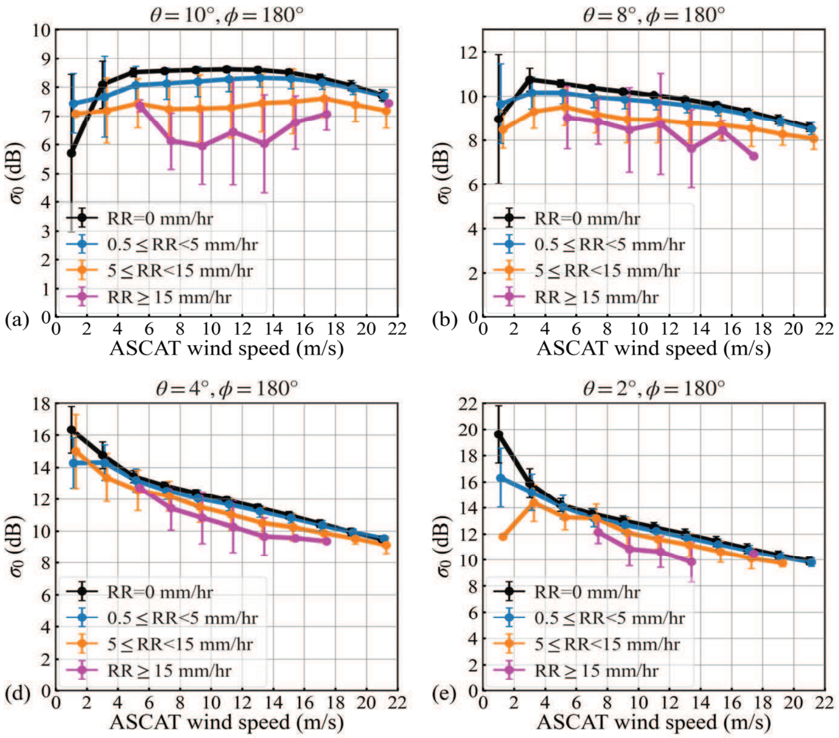

Fig. 15. SWIM NRCS averaged values at incidence angles (a) 10°, (b) 8°, (c) 6°, (d) 4°, and (e) 2°, plotted as a function of ASCAT wind speed under rain-free conditions (black lines) and for three rain rate categories: $0.5 \leq$ RR <5 mm/h (blue), $5 \leq$ RR <15 mm/h (orange), and RR $\geq$ 15 mm/h (magenta). Vertical bars represent the standard deviations within each 2 m/s wind speed bin. Rain rates are obtained from GPM observations.

Rain exerts significant effects on Ku-band radar backscatter, particularly at near-nadir incidence angles, which in turn has important implications for wind retrieval using near-nadir Ku-band instruments such as SWIM. Developing an inversion scheme that accurately retrieves wind under both rain-free and rain-contaminated conditions requires a clear separation between the atmospheric effects and rain-induced modifications to surface roughness. This study serves as an initial step toward that goal. However, to develop a comprehensive model that accounts for both wind and rain, more precise characterization of radar signal modifications in the atmosphere is required. Addressing this will be a primary focus of our future research.

APPENDIX

To facilitate comparison with the dataset based on ECMWF winds, C-band scatterometer winds from ASCAT were collocated with SWIM NRCS under non-TC conditions. Only ASCAT wind measurements that meet the recommended quality flag criteria specified in the product manual and with wind speed below 25 m/s were retained to ensure data reliability. A temporal window of 30 min was applied, and ASCAT winds were cubically interpolated to the center of the SWIM swath. All other spatial and quality control criteria for collocation were maintained consistent with those used for the ECMWF-based dataset. It is important to note that only MetOp-A/ASCAT data, along with GPM and SWIM observations, were available and collocated during the period from January 1 to November 14, 2021, using the 30-min time window, as MetOP-A operations ceased thereafter. For consistency, the SWIM–ECMWF collocated pairs used in the analysis were also restricted to the same time period.

Fig. 15 presents the weighted average of near-nadir SWIM NRCS as a function of ASCAT wind speed in the downwind direction, categorized according to the rain rate groups defined in Section III-A2. Wind speeds were grouped into 2 m/s bins. When comparing the SWIM–ASCAT dataset with the SWIM–ECMWF dataset, the maximum differences in NRCS are generally less than 1.2 dB for wind speeds above 3 m/s and rain rates below 15 mm/h. For rain rates exceeding 15 mm/h, differences range from 1.1 to 2.4 dB, with the ASCAT-based NRCS exhibiting notable fluctuations and occasional data gaps. Furthermore, statistical analyses of NRCS variations with respect to relative wind direction, incidence angle, and rain rate produced conclusions consistent with those derived from the SWIM–ECMWF dataset, reinforcing the robustness of the observed trends.

REFERENCES

[1] D. Hauser, C. Tison, T. Amiot, L. Delaye, N. Corcoral, and P. Castillan, "SWIM: The first spaceborne wave scatterometer," *IEEE Trans. Geosci. Remote Sens.*, vol. 55, no. 5, pp. 3000–3014, May 2017, doi: 10.1109/TGRS.2017.2658672.

[2] D. Hauser et al., "New observations from the SWIM radar on-board CFOSAT: Instrument validation and ocean wave measurement assessment," *IEEE Trans. Geosci. Remote Sens.*, vol. 59, no. 1, pp. 5–26, Jan. 2021, doi: 10.1109/TGRS.2020.2994372.

[3] X. Zhao, L. Oruba, D. Hauser, B. Zhang, and E. Dormy, "What can hurricane sam (2021) tell us about extreme ocean waves under tropical cyclones?" *J. Geophys. Res., Oceans*, vol. 129, no. 8, Aug. 2024, Art. no. e2024JC020957, doi: 10.1029/2024jc020957.

[4] L. Ren, J. Yang, G. Zheng, and J. Wang, "A Ku-band wind and rain backscatter model at low-incidence angles using tropical rainfall mapping mission precipitation radar data," *Int. J. Remote Sens.*, vol. 38, no. 5, pp. 1388–1403, Jan. 2017, doi: 10.1080/01431161.2017.1285081.

[5] X. Qu, Z. Liu, and H. Li, "A backscatter model combing wind and rain effect at low incidence angles," *Mar. Geodesy*, vol. 47, no. 4, pp. 352–366, Jul. 2024, doi: 10.1080/01490419.2024.2313477.

[6] D. Morton, M. Rudman, and J. Liow, "An investigation of the flow regimes resulting from splashing drops," *Phys. Fluids.*, vol. 12, no. 4, pp. 747–763, Apr. 2000, doi: 10.1063/1.870332.

[7] X. Liu, Q. Zheng, R. Liu, D. Wang, J. H. Duncan, and S.-J. Huang, "A study of radar backscattering from water surface in response to rainfall," *J. Geophys. Res., Oceans*, vol. 121, no. 3, pp. 1546–1562, Mar. 2016, doi: 10.1002/2015jc010975.

[8] L. Cavaleri, "Rain, wave breaking and spray," in *Recent Advances in the Study of Oceanic Whitecaps*. Cham, Switzerland: Springer, 2020, ch. 5, pp. 65–75, doi: 10.1007/978-3-030-36371-0_5.

[9] F. T. Ulaby, R. K. Moore, and A. K. Fung, *Microwave Remote Sensing: Active and Passive: Radar Remote Sensing and Surface Scattering and Emission Theory*, vol. 2. Reading, MA, USA: Addison-Wesley, 1982, pp. 457–1064.

[10] D. Atlas, "Footprints of storms on the sea: A view from spaceborne synthetic aperture radar," *J. Geophys. Res., Oceans*, vol. 99, no. C4, pp. 7961–7969, Apr. 1994, doi: 10.1029/94jc00250.

[11] L. F. Bliven, P. W. Sobieski, and C. Craeye, "Rain generated ring-waves: Measurements and modelling for remote sensing," *Int. J. Remote Sens.*, vol. 18, no. 1, pp. 221–228, Jan. 1997, doi: 10.1080/014311697219385.

[12] N. Braun and M. Gade, "Multi-frequency scatterometer measurements on water surfaces agitated by artificial and natural rain," *Int. J. Remote Sens.*, vol. 27, no. 1, pp. 27–39, Jan. 2006, doi: 10.1080/01431160500239214.

[13] M. N. Tsimplis, "The effect of rain in calming the sea," *J. Phys. Oceanogr.*, vol. 22, no. 4, pp. 404–412, Apr. 1992, doi: 10.1175/1520-0485(1992)022<0404:teoric>2.0.co;2.

[14] C. Melsheimer, W. Alpers, and M. Gade, "Simultaneous observations of rain cells over the ocean by the synthetic aperture radar aboard the ERS satellites and by surface-based weather radars," *J. Geophys. Res., Oceans*, vol. 106, no. C3, pp. 4665–4677, Mar. 2001, doi: 10.1029/2000jc000263.

[15] X. Zhao, W. Lin, M. Portabella, Z. Wang, and Y. He, "Effects of rain on CFOSAT scatterometer measurements," *Remote Sens. Environ.*, vol. 274, Jun. 2022, Art. no. 113015, doi: 10.1016/j.rse.2022.113015.

[16] D. Barrick and B. Lipa, "Analysis and interpretation of altimeter sea echo," *Adv. Geophys.*, vol. 27, pp. 61–100, Jan. 1985, doi: 10.1016/S0065-2687(08)60403-3.

[17] Y. Quilfen, J. Tournadre, and B. Chapron, "Altimeter dual-frequency observations of surface winds, waves, and rain rate in tropical cyclone isabel," *J. Geophys. Res., Oceans*, vol. 111, no. C1, Jan. 2006, Art. no. C01004, doi: 10.1029/2005jc003068.

[18] Y. Quilfen, B. Chapron, and J. Tournadre, "Satellite microwave surface observations in tropical cyclones," *Monthly Weather Rev.*, vol. 138, no. 2, pp. 421–437, Feb. 2010, doi: 10.1175/2009mwr3040.1.

[19] X. Xu and A. Stoffelen, "Improved rain screening for Ku-band wind scatterometry," *IEEE Trans. Geosci. Remote Sens.*, vol. 58, no. 4, pp. 2494–2503, Apr. 2020, doi: 10.1109/TGRS.2019.2951726.

[20] K. Zhao, A. Stoffelen, J. Verspeek, A. Verhoef, and C. Zhao, "A conceptual rain effect model for Ku-band scatterometers," *IEEE Trans. Geosci. Remote Sens.*, vol. 61, 2023, doi: 10.1109/TGRS.2023.3264246.

[21] C. Melsheimer, W. Alpers, and M. Gade, "Investigation of multifrequency/multipolarization radar signatures of rain cells over the ocean using SIR-C/X-SAR data," *J. Geophys. Res., Oceans*, vol. 103, no. C9, pp. 18867–18884, Aug. 1998, doi: 10.1029/98jc00779.

[22] D. E. Weissman et al., "Challenges to satellite sensors of ocean winds: Addressing precipitation effects," *J. Atmos. Ocean. Technol.*, vol. 29, no. 3, pp. 356–374, Mar. 2012, doi: 10.1175/jtech-d-11-00054.1.

[23] C. Nie and D. G. Long, "A C-band wind/rain backscatter model," *IEEE Trans. Geosci. Remote Sens.*, vol. 45, no. 3, pp. 621–631, Mar. 2007, doi: 10.1109/TGRS.2006.888457.

[24] W. Alpers, B. Zhang, A. Mouche, K. Zeng, and P. W. Chan, "Rain footprints on C-band synthetic aperture radar images of the ocean–revisited," *Remote Sens. Environ.*, vol. 187, pp. 169–185, Dec. 2016, doi: 10.1016/j.rse.2016.10.015.

[25] B. Zhang and W. Alpers, "The effect of rain on radar backscattering from the ocean," in *Advances in SAR Remote Sensing of Oceans*, 1st ed., Boca Raton, FL, USA: CRC Press, 2018, pp. 325–338.

[26] Y. Zhao, N. Longépé, A. Mouche, and R. Husson, "Automated rain detection by dual-polarization Sentinel-1 data," *Remote Sens.*, vol. 13, no. 16, p. 3155, Aug. 2021, doi: 10.3390/rs13163155.

[27] K. Zhao, A. Stoffelen, J. Verspeek, A. Verhoef, and C. Zhao, "Bayesian algorithm for rain detection in Ku-band scatterometer data," *IEEE Trans. Geosci. Remote Sens.*, vol. 61, 2023, doi: 10.1109/TGRS.2023.3264245.

[28] D. W. Draper and D. G. Long, "Evaluating the effect of rain on Sea-Winds scatterometer measurements," *J. Geophys. Res., Oceans*, vol. 109, no. C12, Dec. 2004, Art. no. C02005.1.

[29] S. N. Nielsen and D. G. Long, "A wind and rain backscatter model derived from AMSR and SeaWinds data," *IEEE Trans. Geosci. Remote Sens.*, vol. 47, no. 6, pp. 1595–1606, Jun. 2009.

[30] M. P. Owen and D. G. Long, "Simultaneous wind and rain estimation for QuikSCAT at ultra-high resolution," *IEEE Trans. Geosci. Remote Sens.*, vol. 49, no. 6, pp. 1865–1878, Jun. 2011.

[31] J. Tournadre and Y. Quilfen, "Impact of rain cell on scatterometer data: 1. Theory and modeling," *J. Geophys. Res., Oceans*, vol. 108, no. C7, p. 3225, Jul. 2003, doi: 10.1029/2002jc001428.

[32] F. Xu, X. Li, P. Wang, J. Yang, W. G. Pichel, and Y.-Q. Jin, "A backscattering model of rainfall over rough sea surface for synthetic aperture radar," *IEEE Trans. Geosci. Remote Sens.*, vol. 53, no. 6, pp. 3042–3054, Jun. 2015, doi: 10.1109/TGRS.2014.2367654.

[33] H. Ye and C. Guo, "A backscattering model of rain-affected sea surface with two-scale method," *IEEE Trans. Geosci. Remote Sens.*, vol. 62, 2024, Art. no. 2005612, doi: 10.1109/TGRS.2024.3428470.

[34] J. Tournadre and J. C. Morland, "The effects of rain on TOPEX/Poseidon altimeter data," *IEEE Trans. Geosci. Remote Sens.*, vol. 35, no. 5, pp. 1117–1135, Sep. 1997, doi: 10.1109/36.628780.

[35] A. Y. Hou et al., "The global precipitation measurement mission," *Bull. Amer. Meteorolog. Soc.*, vol. 95, no. 5, pp. 701–722, May 2014, doi: 10.1175/bams-d-13-00164.1.

[36] G. J. Huffman, E. F. Stocker, D. T. Bolvin, E. J. Nelkin, and J. Tan, *GPM IMERG Final Precipitation L3 Half Hourly 0.1 Degree × 0.1 Degree V07*. Greenbelt, MD, USA: Goddard Earth Science Data Information Services Center (GES DISC), 2023, doi: 10.5067/GPM/IMERG/3B-HH/07.

[37] Federal Meteorological Handbook, "11-doppler radar meteorological observations. Part B: Doppler radar theory and meteorology," Office of the Federal Coordinator Meteorological Services Supporting Res., Washington, DC, USA, Tech. Rep., FCM-H11B-2005, 2005.

[38] D. Rosenfeld, D. B. Wolff, and D. Atlas, "General probability-matched relations between radar reflectivity and rain rate," *J. Appl. Meteorol.*, vol. 32, no. 1, pp. 50–72, Jan. 1993, doi: 10.1175/1520-0450(1993)032<0050:gpmrbr>2.0.co;2.

[39] N. Reul, J. Tenerelli, B. Chapron, D. Vandemark, Y. Quilfen, and Y. Kerr, "SMOS satellite L-band radiometer: A new capability for ocean surface remote sensing in hurricanes," *J. Geophys. Res., Oceans*, vol. 117, no. C2, pp. 1–24, Feb. 2012, doi: 10.1029/2011jc007474.

[40] T. Meissner, L. Ricciardulli, and F. Wentz, *Remote Sensing Systems SMAP daily Sea Surface Winds Speeds on 0.25 deg grid, Version 01.0. [NRT or FINAL]*. Santa Rosa, CA, USA: Remote Sensing Systems, 2018. [Online]. Available: http://www.remss.com/missions/smap/

[41] T. Meissner, L. Ricciardulli, and F. J. Wentz, "Capability of the SMAP mission to measure ocean surface winds in storms," *Bull. Amer. Meteorolog. Soc.*, vol. 98, no. 8, pp. 1660–1677, Aug. 2017, doi: 10.1175/bams-d-16-0052.1.

[42] K. R. Knapp, M. C. Kruk, D. H. Levinson, H. J. Diamond, and C. J. Neumann, "The international best track archive for climate stewardship (IBTrACS): Unifying tropical cyclone data," *Bull. Amer. Meteorolog. Soc.*, vol. 91, no. 3, pp. 363–376, Mar. 2010.

[43] C. Wang et al., "Physics-informed learning for tropical cyclone intensity prediction," *IEEE Trans. Geosci. Remote Sens.*, vol. 62, 2024, Art. no. 5410721, doi: 10.1109/TGRS.2024.3506627.

[44] X. Chu, Y. He, and G. Chen, "Asymmetry and anisotropy of microwave backscatter at low incidence angles," *IEEE Trans. Geosci. Remote Sens.*, vol. 50, no. 10, pp. 4014–4024, Oct. 2012, doi: 10.1109/TGRS.2012.2189010.

[45] Q. Yan, J. Zhang, C. Fan, and J. Meng, "Analysis of Ku{-} and Ka-band sea surface backscattering characteristics at low-incidence angles based on the GPM dual-frequency precipitation radar measurements," *Remote Sens.*, vol. 11, no. 7, p. 754, Mar. 2019, doi: 10.3390/rs11070754.

[46] M. D. Powell et al., "Reconstruction of hurricane Katrina's wind fields for storm surge and wave hindcasting," *Ocean Eng.*, vol. 37, no. 1, pp. 26–36, Jan. 2010, doi: 10.1016/j.oceaneng.2009.08.014.

[47] X. Li, B. Zhang, A. Mouche, Y. He, and W. Perrie, "Ku-band sea surface radar backscatter at low incidence angles under extreme

wind conditions," *Remote Sens.*, vol. 9, no. 5, p. 474, May 2017, doi: 10.3390/rs9050474.

[48] Q. Yan, C. Fan, J. Zhang, and J. Meng, "Understanding Ku-band ocean radar backscatter at low incidence angles under weak to severe wind conditions by comparison of measurements and models," *Remote Sens.*, vol. 12, no. 20, p. 3445, Oct. 2020, doi: 10.3390/rs12203445.

[49] M. A. Donelan, "On the decrease of the oceanic drag coefficient in high winds," *J. Geophys. Res., Oceans*, vol. 123, no. 2, pp. 1485–1501, Feb. 2018, doi: 10.1002/2017jc013394.

[50] M. A. Donelan et al., "On the limiting aerodynamic roughness of the ocean in very strong winds," *Geophys. Res. Lett.*, vol. 31, no. 18, Sep. 2004, Art. no. L18306, doi: 10.1029/2004gl019460.

[51] L. Ren et al., "Ocean surface wind speed dependence and retrieval from off-nadir CFOSAT SWIM data," *Earth Space Sci.*, vol. 8, no. 6, Jun. 2021, Art. no. e2020EA001505, doi: 10.1029/2020ea001505.

Xiaolu Zhao received the B.S. degree in marine sciences from Nanjing University of Information Science and Technology, Nanjing, China, in 2018, where she is currently pursuing the Ph.D. degree in marine meteorology.

Her research interests include microwave scattering numerical simulation, precipitation, and tropical cyclone remote sensing through surface wave investigation and monitoring (SWIM) measurements.

Biao Zhang (Senior Member, IEEE) received the B.S. degree in surveying and mapping engineering from China University of Petroleum, Dongying, China, in 2003, and the Ph.D. degree in physical oceanography from the Institute of Oceanology, Chinese Academy of Sciences, Qingdao, China, in 2008.

He was with the Bedford Institute of Oceanography (BIO), Dartmouth, NS, Canada, from 2008 to 2011, where he was a Post-Doctoral Fellow and was involved in developing synthetic aperture radar, ocean surface wave, and wind retrieval algorithms and products. He is currently a Professor with the School of Marine Sciences, Nanjing University of Information Science and Technology (NUIST), Nanjing, China, and a Visiting Scientist at BIO. He has authored more than 80 peer-reviewed publications and edited two books. His research interests include satellite remote sensing of the marine dynamic environment (wind, waves, currents, and sea ice) and ocean disaster monitoring (tropical cyclones, polar lows, and oil spills), and air-sea interactions under extreme weather conditions. He is also interested in marine big data and artificial intelligence (AI) oceanography.

Dr. Zhang was a recipient of the Visiting Fellow Scholarship of Natural Sciences and Engineering Research Council of Canada (NSERC) in 2008 and the Excellent Young Scientist Award by the National Natural Science Foundation of China in 2016. He received the First Award of Science and Technology of Jiangsu Province in 2017, the First Award of Ocean Science and Technology of the State Oceanic Administration of China, and the Second Award of Natural Science of the Ministry of Education of China in 2014, as well as the Second Award of Natural Resource Science and Technology in 2022. He was selected as the "Six Talent Summit" and "333 High Talent Engineering" of Jiangsu Province in 2018 and 2021, respectively.

Ludivine Oruba received the Ph.D. degree in meteorology from Université Pierre et Marie Curie, Paris, France, in 2012.

She has been an Associate Professor at Sorbonne Université, Paris, France, since 2017. Her previous work has explored the dynamics of mid-latitude storms and the magnetohydrodynamic flow of liquid metal within Earth's core, which generates the planet's magnetic field. Her research focuses on the dynamics of geophysical fluids, specifically the atmosphere and the ocean. She has a particular interest in tropical cyclones, including their formation, intensification mechanisms, and the influence of cyclonic swell on coral islands.

Alexis Mouche received the Ph.D. degree in ocean remote sensing from the Université de Versailles Saint-Quentin, Versailles, France, in 2005.

He has been a Senior Research Scientist with the Laboratoire d'Océanographie Physique et Spatiale, Institut Francais de Recherche pour l'Exploitation de la Mer, Plouzane, France, since 2014. His research interests include the interaction of electromagnetic and oceanic waves for ocean remote sensing applications.

Danièle Hauser (Senior Member, IEEE) received the Ph.D. degree in meteorology from Université Paris VII, Paris, France, in 1980, and the State Thesis degree in physics from the University Pierre and Marie Curie, Paris, in 1989.

She is currently an Emeritus Researcher at the Centre National de la Recherche Scientifique (CNRS) and develops her activity at the Laboratoire Atmosphère, Milieux, Observations Spatiales (LATMOS), Guyancourt, France. After starting her research career in the field of meteorology and cloud physics using radar observations, she has been working for more than 35 years on microwave observations of the ocean surface (surface wind, waves, and salinity) and air/sea interactions studies. Until 2022, she was the Principal Investigator of the CFOSAT mission dedicated to the global measurement of wind and waves from satellite, and is currently its Co-Principal Investigator.